JGR Oceans

RESEARCH ARTICLE
10.1029/2022JC018952

Key Points:

- Forward Greenland tip jets trigger oceanic upwelling along the southwest coast of Greenland
- The wind-induced upwelling fluxes freshwater offshore at the surface and heat onshore at depth via the cross-stream Ekman circulation
- The freshwater flux could inhibit wintertime convection in the eastern basin, thus explaining why Labrador Sea Water is not formed there

Correspondence to:
A. Pacini,
astrid.pacini@gmail.com

Citation:
Pacini, A., & Pickart, R. S. (2023). Wind-forced upwelling along the west Greenland shelfbreak: Implications for Labrador Sea Water formation. *Journal of Geophysical Research: Oceans*, *128*, e2022JC018952. https://doi.org/10.1029/2022JC018952

Received 7 JUN 2022
Accepted 15 FEB 2023

Wind-Forced Upwelling Along the West Greenland Shelfbreak: Implications for Labrador Sea Water Formation

Astrid Pacini[1,2] and Robert S. Pickart[1]

[1]Woods Hole Oceanographic Institution, Woods Hole, MA, USA, [2]Now at Applied Physics Laboratory, University of Washington, Seattle, WA, USA

Abstract Arctic-origin and Greenland meltwaters circulate cyclonically in the boundary current system encircling the Labrador Sea. The ability of this freshwater to penetrate the interior basin has important consequences for dense water formation and the lower limb of the Atlantic Meridional Overturning Circulation. However, the precise mechanisms by which the freshwater is transported offshore, and the magnitude of this flux, remain uncertain. Here, we investigate wind-driven upwelling northwest of Cape Farewell using 4 years of high-resolution data from the Overturning in the Subpolar North Atlantic Program west Greenland mooring array, deployed from September 2014–2018, along with Argo, shipboard, and atmospheric reanalysis data. A total of 49 upwelling events were identified corresponding to enhanced northwesterly winds, followed by reduced along-stream flow of the boundary current and anomalously dense water present on the outer shelf. The events occur during the development stage of forward Greenland tip jets. During the storms, a cross-stream Ekman cell develops that transports freshwater offshore in the surface layer and warm, saline, Atlantic-origin waters onshore at depth. The net fluxes of heat and freshwater for a representative storm are computed. Using a one-dimensional mixing model, it is shown that the freshwater input resulting from the locus of winter storms could significantly limit the wintertime development of the mixed layer and hence the production of Labrador Sea Water in the southeastern part of the basin.

Plain Language Summary The western Labrador Sea is one of the few locations in the world ocean where open-ocean convection forms intermediate waters. This happens when strong winds and large air-sea heat fluxes densify surface waters and mix them to depth. The presence of surface freshwater can inhibit this process, and, curiously, the deepest convection occurs in the western Labrador Sea even though the wintertime air-sea fluxes are comparable in the eastern Labrador Sea. In this study, we use 4 years of temperature, salinity, and velocity mooring data and atmospheric reanalysis data from the west Greenland shelf and slope to demonstrate that freshwater is transported from the shelf to the interior eastern Labrador Sea due to short, intense storms known as forward Greenland tip jets. The strong winds set up a temporary cross-stream circulation called an Ekman cell that transports freshwater offshore in the surface layer and heat onshore at depth. Over the 4 years, 49 such events were observed, which we describe and characterize. Importantly, we show that during the winter season, these storms flux enough freshwater offshore to inhibit the densification of surface waters in the eastern Labrador Sea, thus explaining why deep convection is only observed in the west.

1. Introduction

The Labrador Sea, and the formation of the intermediate ventilated water mass known as Labrador Sea Water (LSW), play an important role in the Atlantic Meridional Overturning Circulation (AMOC; e.g., Rhein et al., 2002; Sy et al., 1997; Talley & McCartney, 1982). The formation of this water mass through open ocean convection and the spreading of these newly ventilated waters via boundary currents (Dickson & Brown, 1994; Fischer et al., 2010; Georgiou et al., 2021; Pickart, 1992) and interior pathways (Bower et al., 2009; Lavender et al., 2000) have important implications for the circulation of the subpolar gyre as well as the sequestration of carbon from the atmosphere to the ocean (Khatiwala et al., 2013; Takahashi et al., 2009).

LSW production is driven by buoyancy exchange at the air-sea interface (e.g., R. A. Clarke & Gascard, 1983; Lab Sea Group, 1998). In the western Labrador Sea, it is formed by air-sea heat fluxes that result from low-pressure systems that advect cold air off the Labrador land mass and extract buoyancy from the surface waters (e.g., Pickart et al., 2002; Schulze et al., 2016). A water mass indistinguishable from LSW is also formed in the southwest Irminger Sea (e.g., De Jong et al., 2012; Pickart, Spall, et al., 2003; Piron et al., 2017; Våge et al., 2008).

The convection there is more tightly coupled to the presence of the forward Greenland tip jet (Pickart, Spall, et al., 2003; Våge et al., 2008), an atmospheric phenomenon that occurs when low-pressure systems following the North Atlantic storm track impinge on the high topography of southern Greenland. As this happens, air parcels accelerate around the tip of Greenland (Våge et al., 2009), resulting in large air-sea heat fluxes and wind stresses in a localized region east of Cape Farewell (e.g., Doyle & Shapiro, 1999; Moore, 2003; Moore & Renfrew, 2005). Various observations also point to LSW production within a small recirculation gyre in the southeastern Labrador Sea (Lavender et al., 2000; Pickart & Spall, 2007; Zunino et al., 2020). Deep wintertime mixed layers have also been measured within the boundary current system of east Greenland (Le Bras et al., 2020) and along the Labrador slope (Pickart et al., 2002).

The strength of convection and annual production of LSW depend not only on the strength of the surface forcing, but also on the preconditioning of the water column prior to the winter season (e.g., Lilly et al., 1999). The strength of the stratification in the interior basin dictates the amount of energy required to penetrate the surface layer and homogenize the underlying water. For this reason, it is critical to understand the processes responsible for pre-conditioning the water column prior to deep convection, and for restratifying the water column after periods of strong ventilation (Chanut et al., 2008; Gelderloos et al., 2011; Katsman et al., 2004; Lilly & Rhines, 2002; Lilly et al., 2003, 1999). This stratification is predominantly dictated by the water mass composition of the boundary currents and the offshore flux of properties from these currents (Hátún et al., 2007; Lilly & Rhines, 2002; Lilly et al., 2003, 1999; Prater, 2002; Straneo, 2006).

The cyclonic boundary current system that circumnavigates the Labrador Sea is composed of three branches on the east (west) side of the basin: the West Greenland Coastal Current (Labrador Coastal Current) that advects cold and fresh meltwaters of both Arctic and Greenland origin on the inner shelf (WGCC/LCC; Florindo-López et al., 2020; Lin et al., 2018); the West Greenland Current (Labrador Current) which advects warm, saline, Atlantic-origin water at depth and cold and fresh melt waters at the surface (WGC/LC; Colbourne et al., 1994; Cuny et al., 2002; Myers et al., 2009, 2007; Rykova et al., 2015); and the Deep Western Boundary Current that advects overflow waters ventilated in the Nordic Seas at depth (DWBC; Dickson & Brown, 1994; Figure 1). Mesoscale to submesoscale variability is responsible for the offshore transport of properties from the surface and middepth components of the boundary currents into the interior (e.g., Chanut et al., 2008; Eden & Böning, 2002; Gascard & Clarke, 1983; Lilly et al., 2003, 1999; Prater, 2002; Rieck et al., 2019; Thomsen et al., 2014).

The strong eddy kinetic energy signature in the Labrador Sea can be subdivided into four main categories: Irminger Rings (IRs); Convective Eddies (CEs); Boundary Current Eddies (BCEs); and Denmark Strait Overflow Water (DSOW) cyclones. For a summary of these different eddy signatures, the reader is referred to Pacini and Pickart (2022), who also present the first observational evidence of BCEs along the west Greenland continental slope. Together, the IRs and BCEs transport cold, fresh water near the surface and warm, saline water at depth from the WGC into the basin, both of which can influence interior winter mixed layer development (Chanut et al., 2008; Katsman et al., 2004; Kawasaki & Hasumi, 2014; Lilly et al., 2003; Pennelly & Myers, 2020). While some studies are able to account for most of the necessary heat transport from the boundary current to the interior via eddy mechanisms (e.g., Katsman et al., 2004; Lilly et al., 2003), to date no studies can account for the freshwater transport needed to balance the interior Labrador Sea freshwater budget annually (Hátún et al., 2007; Lilly et al., 2003; Schulze Chretien & Frajka-Williams, 2018; Straneo, 2006).

In addition to the intrinsic eddy variability within the Labrador Sea, there is strong wind forcing; to wit, Cape Farewell is the windiest place in the World Ocean (Moore et al., 2008; Sampe & Xie, 2007). Various modeling studies have addressed the role of winds in the export of freshwater from the surface WGC and WGCC into the interior Labrador Sea. For instance, Castelao et al. (2019) and Luo et al. (2016) find a preferential pathway for meltwater originating along east Greenland to be fluxed offshore due to wind events, as compared to meltwater originating along west Greenland, which tends to enter Baffin Bay along the shelf. Luo et al. (2016) stress that large variability in wind forcing could explain changes in freshwater export on interannual timescales. In particular, the orientation of the predominant winds during the melt season (May–September) has a large impact on the offshore export of meltwaters: years with upwelling favorable winds exhibit a large offshore freshwater signal, whereas years with downwelling-favorable winds constrain meltwater to the coast.

The model results of Böning et al. (2016) demonstrated that meltwater entering the Labrador Sea from the west Greenland shelf has caused a small but significant freshening trend at the surface of the Labrador Sea that has not yet influenced AMOC but could in the future, as more freshwater fills the west Greenland shelf. Schulze

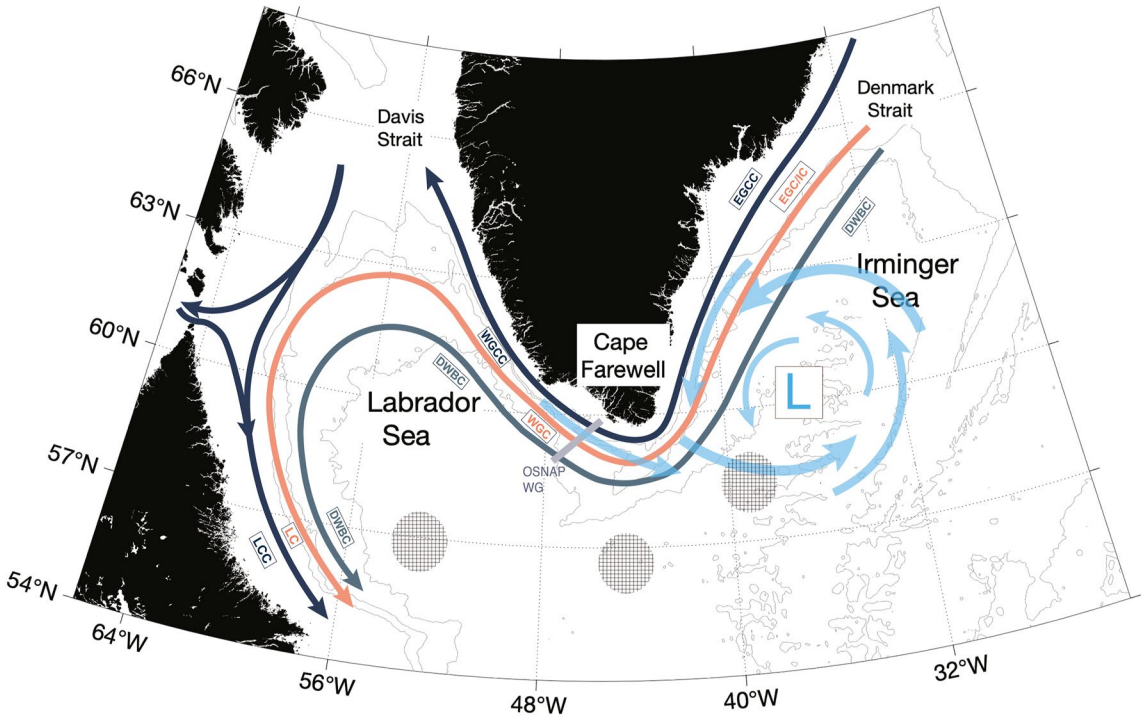

Figure 1. Schematic circulation of the boundary current system in the Labrador and western Irminger Seas. EGCC is the East Greenland Coastal Current; EGC/IC is the East Greenland Current/Irminger Current; DWBC is the Deep Western Boundary Current; WGCC is the West Greenland Coastal Current; WGC is the West Greenland Current; LCC is the Labrador Coastal Current; LC is the Labrador Current. The gray line across the boundary current system indicates the location of the OSNAP west Greenland mooring array. The hatched areas schematically represent the regions of deep convection in the Labrador and Irminger Seas. Also shown is the schematic wind field of a low-pressure system triggering a forward tip jet in the vicinity of Cape Farewell and also causing barrier winds along the southeast Greenland coast.

Chretien and Frajka-Williams (2018) performed a Lagrangian analysis using a high-resolution 1/12° ocean model to demonstrate that 60% of the freshwater in the top 100 m in the interior basin emanates from the top 30 m of the west Greenland shelf due to Ekman transport versus eddy processes. While Castelao et al. (2019) also showed that upwelling-favorable winds transport meltwater from the shelf into the WGC, the freshwater is subsequently fluxed into the interior basin by eddies. Additionally, recent modeling work along southeast Greenland and at Cape Farewell demonstrates that forward Greenland tip jets and westerly wind events flux a substantial amount of liquid freshwater across the shelfbreak at synoptic timescales east and south of Cape Farewell (Duyck et al., 2022).

From the observational perspective, drifter tracks near Cape Farewell show that freshwater is diverted seaward from the coast on both sides of Greenland, likely due to wind (Duyck & De Jong, 2021). Similarly, Majumder et al. (2021) used satellite and historical in-situ data from shipboard casts, Argo floats, gliders, and moorings to investigate freshwater fluxes into the Labrador Sea on seasonal to interannual timescales. They documented a substantial westward transport of freshwater from southwest Greenland between 60°–62°N and 63°–64.8°N due to the large-scale, geostrophically balanced flow coincident with the 1,000–2,000 m isobaths. Holliday et al. (2007) provide further evidence for the export of freshwater offshore at Cape Farewell by using a synoptic hydrographic survey to document that the EGC transport reduces by 5.1 Sv as it rounds Cape Farewell.

To date, none of the models or observational studies address the role of synoptic-scale wind events on the freshwater budget of the interior Labrador Sea. Synoptic-scale low-pressure systems are responsible for a variety of high-speed wind events in the vicinity of Cape Farewell, including forward tip jets, reverse tip jets, and barrier winds (e.g., Moore & Renfrew, 2005). The type of event depends on the angle of impingement of the low relative to the orography of southern Greenland. Forward tip jets are characterized by a narrow band of strong westerly winds extending from Cape Farewell across the Irminger Sea, while reverse tip jets have a similarly narrow band of strong easterly winds extending from Cape Farewell across the Labrador Sea (Moore & Renfrew, 2005). Barrier winds are enhanced flow banked against the high topography of the east coast of Greenland (Moore & Renfrew, 2005).

Studies have shown that forward tip jet and reverse tip jet frequency is elevated in years of high North Atlantic Oscillation (Bakalian et al., 2007; Våge et al., 2009) when the North Atlantic storm track is shifted to the northeast, making low-pressure impingement on southern Greenland more likely (Moore, 2003; Pickart, Spall, et al., 2003).

In this paper, we investigate the wind-driven variability of the WGC using 4 years of data from a high-resolution mooring array situated west of Cape Farewell, along with Argo data and atmospheric reanalysis data. We focus on upwelling events driven by synoptic storms, which are frequent during the cold season. We begin by presenting the method for identifying the events, and then present their statistics. Following this, we describe the kinematic and hydrographic response, including a case study of a single event. The nature of the atmospheric forcing is then investigated, followed by quantification of the cross-stream fluxes of heat and freshwater induced by the resulting Ekman cell. Lastly, we explore the impacts of this wind-driven freshwater flux on interior convection in the Labrador Sea.

2. Data and Methods

2.1. Mooring Data

The mooring data used in this study consist of 4 years of hourly pressure, temperature, salinity, and velocity measurements from the 10 moorings that comprise the Overturning in the Subpolar North Atlantic Program (OSNAP) west Greenland array (Lozier et al., 2019; Pacini et al., 2020; Figure 1). The moorings cover the shelf and slope of the eastern Labrador Sea near 59°N, from 130 m water depth on the shelf to the 3,000 m isobath at the offshore end of the array. The moorings sample the DWBC, the WGC, and the seaward side of the WGCC (Figure 2). They were first deployed in August 2014, were serviced again in 2016, 2018, 2020, and 2022, and remain in the water to date. The array consists of three shelf tripods (LS1–LS3), five full-depth moorings (LS4–LS8), and two bottom-instrumented moorings (DSOW3–DSOW4) that together have 49 Sea-Bird SBE37 MicroCATs measuring pressure, temperature, and conductivity; 33 Nortek Aquadopps measuring point-values of velocity; and eight acoustic Doppler current profilers (RDI ADCPs, 300 and 75 kHz) measuring vertical profiles of velocity (Figure 2). The moorings are spaced on average 15 km apart. After the 2018 turnaround, additional tripods were deployed inshore of LS1 on the shelf. In this study, we use data from LS1–LS8 over the time period 2014–2018.

Vertical sections of potential temperature referenced to the surface (hereafter referred to as temperature), salinity, potential density referenced to the surface (hereafter referred to as density), and along- and cross-stream velocity were created for each time step with Laplacian-Spline interpolation (Smith & Wessel, 1990). For the full mooring array, the gridded product has 5 km resolution in the horizontal and 100 m resolution in the vertical. The velocity data were de-tided using the harmonic tidal routine T_TIDE (Pawlowicz et al., 2002) and rotated such that the cross-stream transport was minimized. Positive along-stream velocity u is towards the north-west, and positive cross-stream velocity v is directed offshore (southwest). The processing, accuracy, de-tiding, rotating, and gridding are described in detail by Pacini et al. (2020). Additionally, in this study, we take advantage of the high vertical resolution of the ADCPs to create a finer grid with 10 km horizontal resolution and 20 m vertical resolution for along- and cross-stream velocity on the shelf and near the shelfbreak, in the subset of the domain shown by the green box in Figure 2. We use both of the gridded products in the study, as well as individual timeseries from the instruments.

2.2. Atmospheric Data

The atmospheric data used in the study are from the European Centre for Medium Range Weather Forecasting (ECMWF) ERA5 atmospheric reanalysis product (Figure 3; Hersbach et al., 2020). The product has 0.25° resolution in both latitude and longitude, and hourly temporal resolution. We consider the following variables: sea level pressure (SLP), 10 m zonal and meridional winds, 2 m air temperature, and heat flux components (latent, sensible, solar, and long-wave). Earlier studies have shown good agreement between observations and Integrated Forecast System-based reanalysis products around Greenland (Renfrew et al., 2002, 2009). We subsample the data to every 3 hr.

2.3. Shipboard Data

Shipboard hydrographic measurements from two cruises are used to provide high-resolution vertical profiles of temperature and salinity. In particular, we use conductivity-temperature-depth (CTD) casts from a 1997 winter survey of the Labrador Sea carried out by R/V *Knorr* (see Pickart et al., 2002 for details) and from a 2018 fall survey of the west Greenland boundary current system carried out by R/V *Neil Armstrong*. The winter survey was conducted from 2 February to 20 March 1997, and the fall survey was conducted from 27 August to 2 October 2018. The reader is referred to Pickart et al. (2002) for details of the data processing and sensor accuracy for the

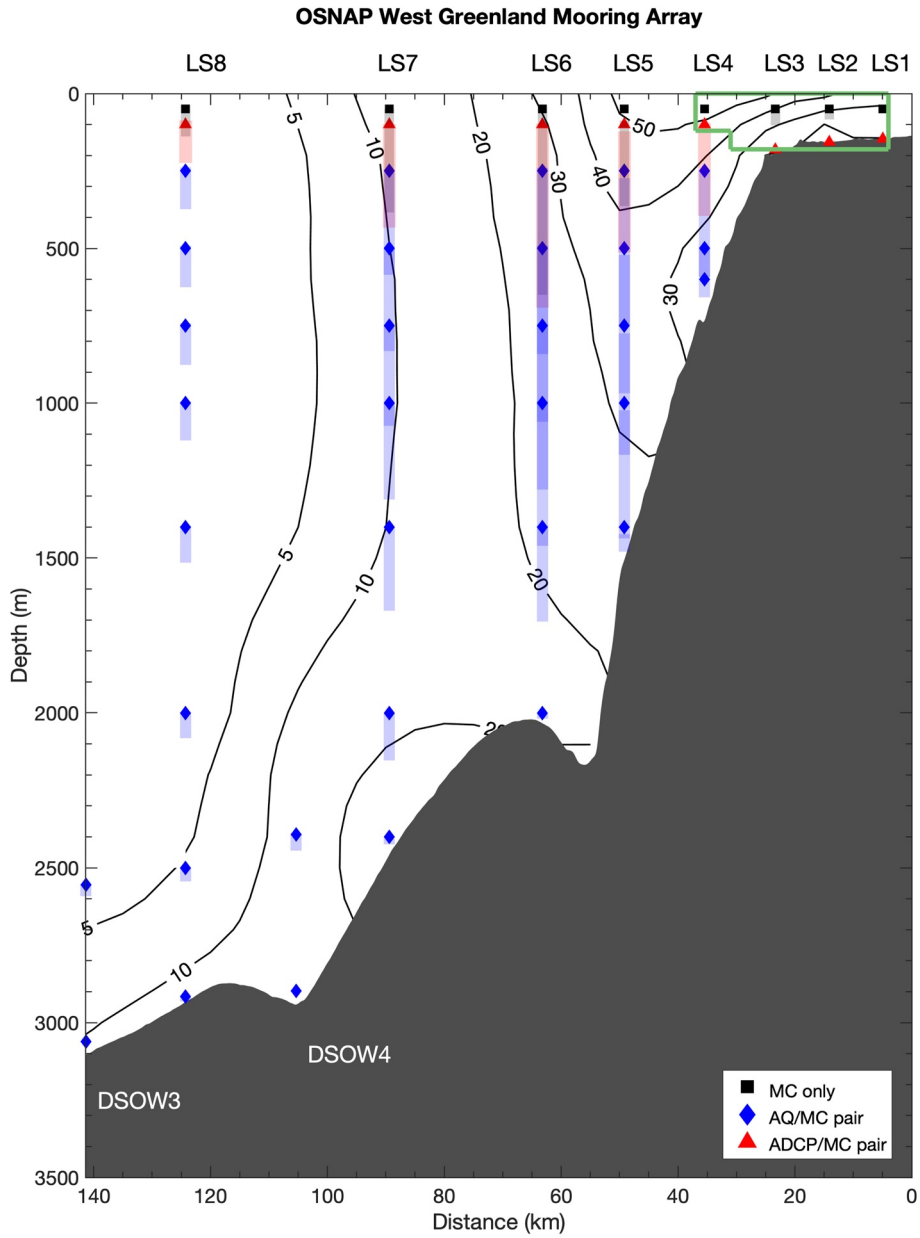

Figure 2. Vertical section showing the mooring array instrument configuration (from Pacini et al., 2021). The solid symbols denote the instrument deployment locations, and the shading indicates the depth range over which instruments sampled due to mooring blowdowns. MicroCATs are MC; Aquadopps are AQ. The mean section of along-stream velocity is contoured (cm/s, positive values indicate flow to the northwest). The green polygon denotes the region within which the higher-resolution velocity grid is constructed.

wintertime survey. The fall survey used a Sea-Bird 911+ CTD mounted on a frame with 24 10-L Niskin bottles. The temperature sensors were calibrated at Sea-Bird, and the conductivity sensors were calibrated using water sample salinity measurements collected during the cruise. The estimated accuracy for temperature and salinity for the fall cruise is 0.001°C and 0.002, respectively.

2.4. Interior Labrador Sea Data

All Argo profiles within the western Labrador Sea (defined as the region from 57°–59.5°N to 52°–55°W) and within the recirculation gyre in the southeastern Labrador Sea (defined as the region from 57.6°–59.5°N to 45°–49.5°W and within the −8 cm absolute dynamic topography contour) from November 2014 were downloaded

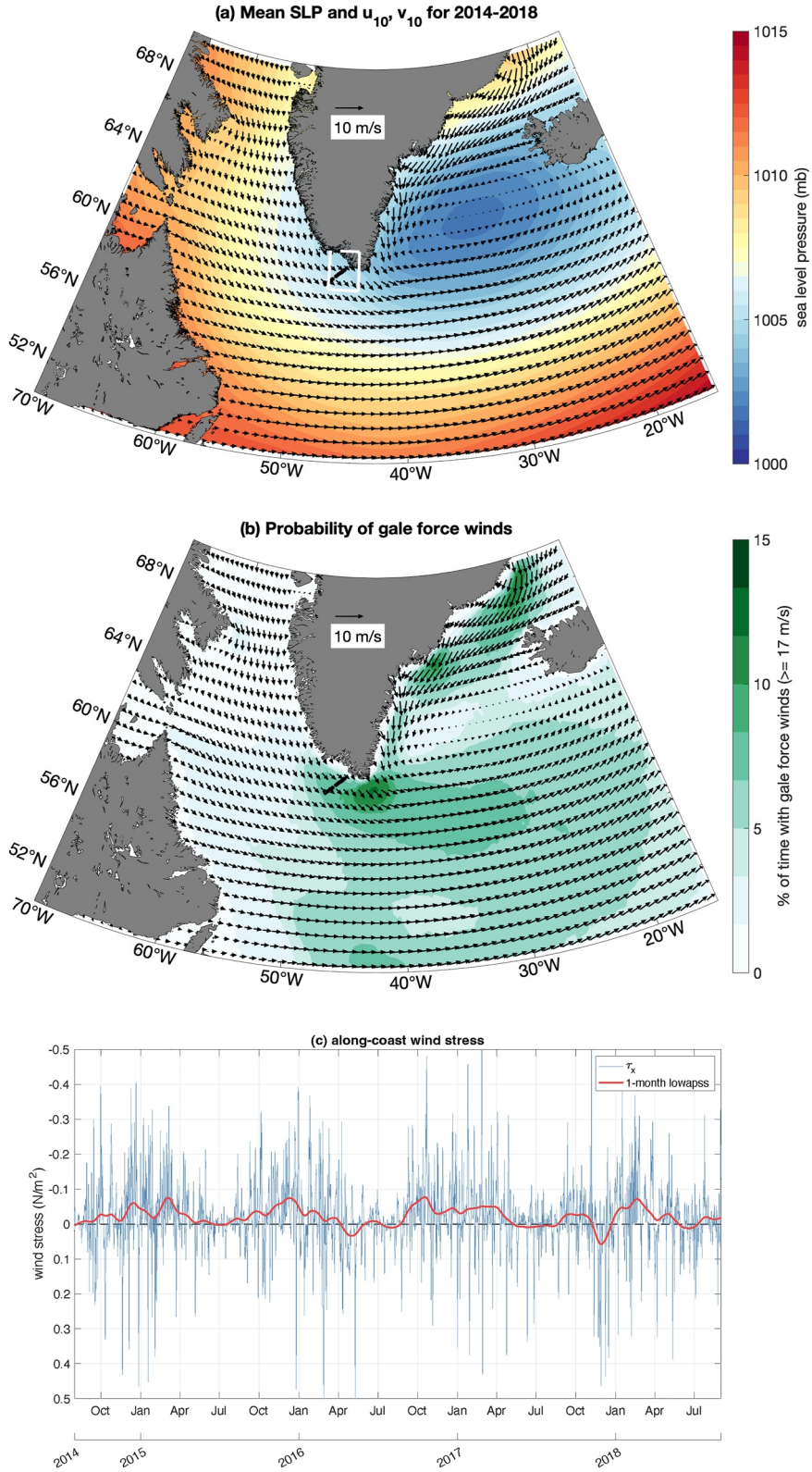

Figure 3. (a) 2014–2018 mean sea level pressure (color) and 10 m wind vectors from ERA5. Every third wind vector is shown. The black line indicates the OSNAP west Greenland mooring array. The white box denotes the domain over which the along-coast winds were averaged (see text for details). (b) Percentage of time subject to gale force winds (>17 m/s) over the time period 2014–2018, with the mean 10 m wind vectors from (a) overlaid. (c) Timeseries of along-coast wind stress (τ_x) within the white box in (a). Upwelling favorable wind stress is negative (note the inverted axis).

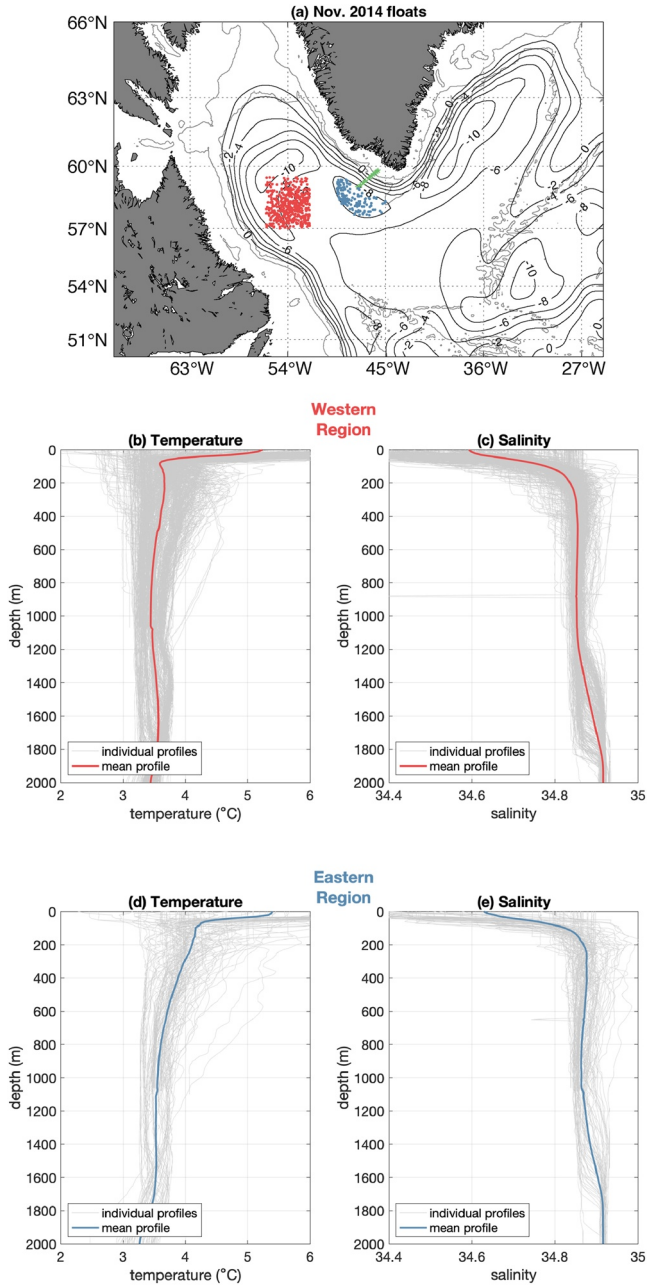

Figure 4. (a) Locations of all Argo profiles in the western Labrador Sea (red dots) and within the recirculation gyre in the eastern Labrador Sea (blue dots). The contours of mean absolute geostrophic pressure at 700 m from Lavender et al. (2000) are shown in black, and the bathymetric contours are shown in gray. The green stars denote the moorings of the OSNAP west Greenland array. (b) Mean November profile of temperature within the western Labrador Sea (red curve), with all available profiles shown in light gray. (c) Same as (b) except for salinity. (d) Same as (b) except for the eastern recirculation gyre. (e) Same as (c) except for the eastern recirculation gyre.

(see Figure 4a). The data are made freely available by the International Argo Program (Argo, 2021) and the national programs that contribute to it (https://argo.ucsd.edu, https://www.ocean-ops.org). The Argo Program is part of the Global Ocean Observing System. We excluded profiles that exhibited unrealistic spikes in salinity (salinity < 33). This resulted in 676 profiles from 17 floats in the western Labrador Sea, and 669 profiles from 14 floats within the recirculation gyre. These individual profiles were gridded at 10 m vertical resolution, then averaged together to create mean profiles of temperature and salinity within the western Labrador Sea (Figures 4b and 4c) and in the eastern recirculation gyre (Figures 4d and 4e). Sensitivity tests were run by selecting a subset of profiles to see if the general vertical structure of the average profile changed, but there were no substantial differences among the composite profiles.

2.5. One-Dimensional Mixed Layer Model

To study the wintertime evolution of the mixed layer in the interior Labrador Sea, the one-dimensional mixing model of Price et al. (1986) is used (hereafter referred to as PWP). The model is initialized with the average Argo temperature and salinity profiles from Figure 4 and forced with the atmospheric heat flux and wind stress timeseries from ERA5, extracted from the same domain as the Argo profiles (see Section 2.4 for domain boundaries). At each timestep, the model calculates the bulk and gradient Richardson numbers to adjust the density profile until static stability has been achieved. For the purposes of the following analysis, the mixed layer is defined as the first location where the vertical density gradient exceeds 0.5×10^{-3} kg/m^3.

3. Results

3.1. Diagnosing Upwelling Events

The NAO index was strongly positive during the study period (2014–2018), indicating a strengthened SLP gradient between the Icelandic Low and the Azores High. A strong positive NAO is associated with more frequent and stronger storms and a northward shift in the North Atlantic storm track (e.g., Moore, 2003; Rogers, 1990; Serreze et al., 1997), which resulted in upwelling-favorable winds over the 2014–2018 mooring deployment period (Figure 3c). It is thus likely that the increased occurrence of synoptic storms could energize the boundary current system and induce a water column response beyond the seasonal and interannual mean wind fields described in the modeling literature (e.g., Böning et al., 2016; Luo et al., 2016). Figure 3b shows the probability of gale force winds within the subpolar gyre. Two regions of strong storm activity are evident: a band along the east coast of Greenland associated with the barrier winds (with local enhancement near 64°N and 68°N), and one at the southern tip of Greenland, where forward tip jets and reverse tip jets occur (Moore & Renfrew, 2005). Many studies have examined the connection between forward tip jets and the hydrographic conditions east of Greenland (e.g., Josey et al., 2019; Pickart, Spall, et al., 2003; Våge et al., 2008), but observations describing how these storms affect the west coast of Greenland are lacking.

Here, we objectively define upwelling events using the mooring and reanalysis data as follows. First, the density anomaly at the base of the water column is computed for all three shelf tripods (LS1–LS3; see Figure 2) by subtracting the 30-day lowpass of density from each hourly measurement for the respective MicroCATs. This removes any seasonal biases in the anomaly signature (see also Foukal et al., 2019; Lin et al., 2019). The three anomalies are then averaged together at each time step, providing an hourly density anomaly at the base of the water column on the outer west Greenland

shelf. (The results below are not sensitive to the choice of mooring for the density anomaly.) Next, the analogous calculation is performed to obtain a timeseries of along-stream velocity anomaly; in this case, the timeseries is depth-averaged over the water column. Finally, we compute a timeseries of average along-coast wind speed within the box shown in Figure 3a, where the rotation angle is the same as that used for the ocean velocity (see Section 2.1 for details). Again, the 30-day lowpass was subtracted to create an anomaly timeseries.

Previous studies of shelfbreak upwelling in the Arctic Ocean (e.g., Lin et al., 2016) have found a lag between the hydrographic and velocity signatures relative to the wind forcing. In particular, the velocity response lags the wind, followed later by the response of the density. We thus computed the lagged correlations between our three timeseries to understand their relative signatures. This revealed that, over the 4 yr record, the wind leads the ocean velocity response by 6–9 hr, and the ocean velocity response leads the ocean density response by 12–15 hr (these are similar to the lags found by Lin et al., 2019 for the shelfbreak jet of the Beaufort Sea). Note also that a comparison of wind speeds along west and east Greenland indicates that wind conditions along west Greenland lead wind conditions along east Greenland by 3 hr (discussed further below).

Guided by the lagged correlations, we defined an upwelling event based on the following criteria: for every time period associated with a positive density anomaly greater than 0.05 kg/m^3, we stipulate that, in the temporal range spanning 24 hr before the onset of the anomaly to 24 hr after the onset of the anomaly, 12 of those hours must have a negative along-stream velocity anomaly (i.e., the northward-flowing boundary current weakens). Additionally, we require 12 of the hours spanning the time period 48 hr before the onset of the density anomaly to 24 hr after the onset of the anomaly to have a negative anomaly in along-coast winds (i.e., enhanced northwesterlies). Finally, the density anomaly must last for at least 48 hr. While this set of criteria are taken to be the most effective for objectively identifying the upwelling events, we stress that the results below are not sensitive to the detailed definitions. When the four criteria are applied, 49 upwelling events between September 2014 and September 2018 are identified, as shown in Figure 5. These occur predominantly during the winter months.

It is important to note that, upon inspection of each event, we are able to distinguish between upwelling events driven by the passage of one low-pressure system versus events produced by a train of cyclones. Such trains of low-pressure systems act to keep the bottom density elevated for longer periods of time than in the single-storm scenario. In the subsequent analysis, we distinguish between events associated with a single storm versus multiple storms.

3.2. General Characteristics of Upwelling Events

3.2.1. Effect of Wind

For each of the 49 upwelling events identified using the above set of metrics, a storm-dependent rotation angle was computed for the depth-averaged water column flow. This was necessary in order to more effectively identify the cross-stream Ekman cell for each event (see also Schulze & Pickart, 2012). The storm-dependent rotation angle was defined as the direction of the mean flow in the center half of the storm event (i.e., between 1/4 of the way through the storm to 3/4 of the way through the storm). On average, the rotation angles only deviate from the original orientation of the flow by 3.2°.

We assess the relative strength of each event and its correlation to the along-coast winds by computing the upwelling index (UI) following Lin et al. (2019) and the cumulative velocity anomaly (CVA) following Ovall et al. (2021), and then compare them to the cumulative Ekman transport (Huyer et al., 1979). The UI is defined as the integral in time of the bottom density anomaly over the course of the event,

$$\mathrm{UI} = \int_{t_s}^{t_e} \rho_a dt,$$

where ρ_a is the bottom density anomaly, and t_s and t_e are the start and end times of the event, defined as when the bottom density anomaly crosses above and below 0.05 kg/m^3, respectively. Similarly, the CVA is defined as the time integral of the velocity anomaly

$$\mathrm{CVA} = \frac{1}{H} \int_{t_s - t_v}^{t_e - t_v} v_a dt,$$

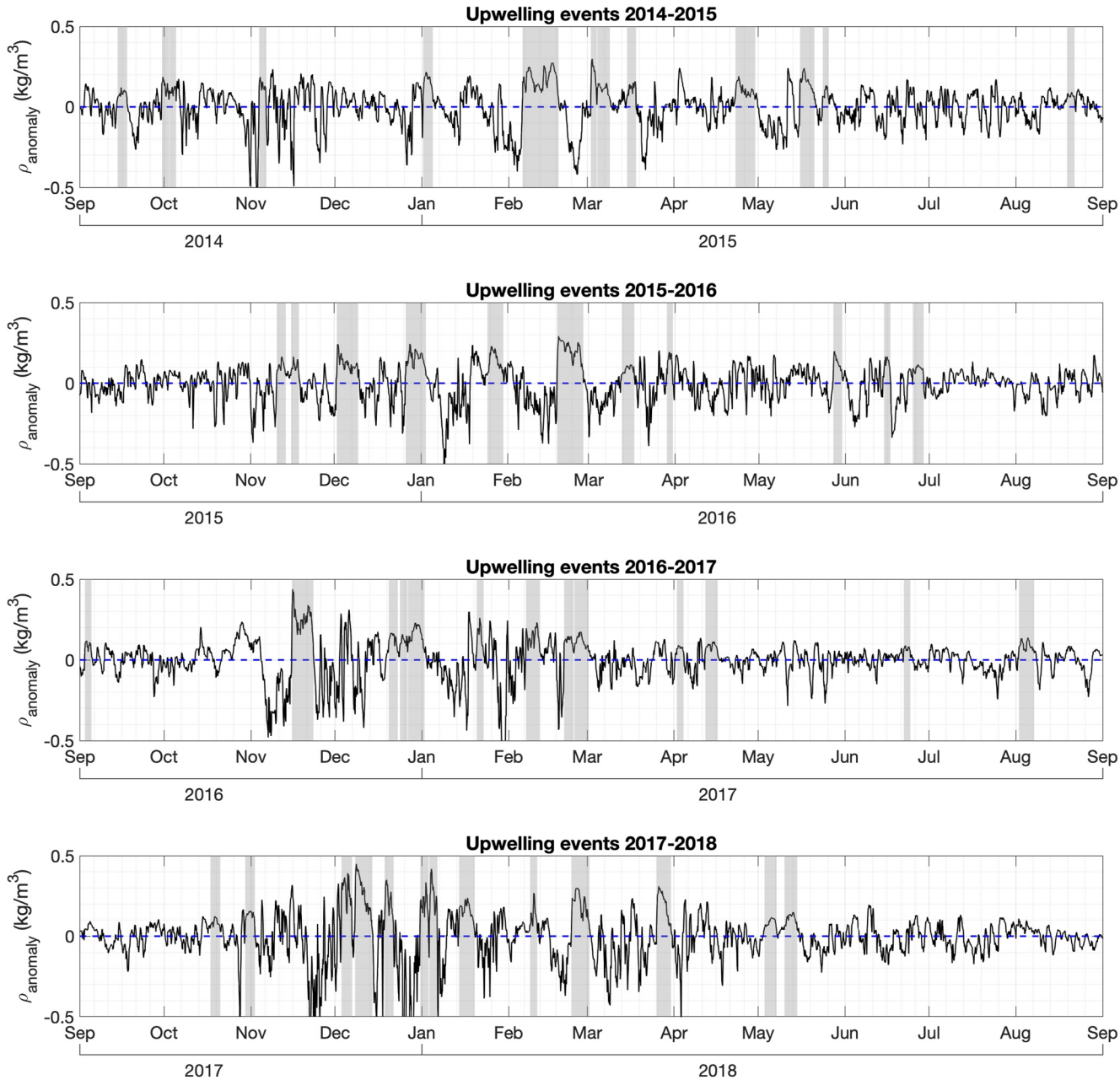

Figure 5. Timeseries of bottom density anomaly averaged between tripods LS1–LS3, over the 4 yr deployment (2014–2018). The upwelling events are indicated by gray shading (see text for details on defining the upwelling periods).

where H is the bottom depth, v_a is the depth-averaged velocity anomaly, and t_v is the average lag (9 hr) between the wind signal and the velocity response of the water column. The cumulative Ekman transport (T_{CE}) is defined as follows:

$$T_{CE} = \int_{t_s - t_h}^{t_e - t_h} \tau_s(t) dt / \rho_0 f,$$

where τ_s is the along-coast wind stress, f is the Coriolis parameter, ρ_0 is the reference density 1,025 kg/m^3, and t_h is the average lag (18 hr) between the hydrographic response of the water column and the wind. Note that UI, CVA, and T_{CE} take into account both the duration and the strength of the upwelling event.

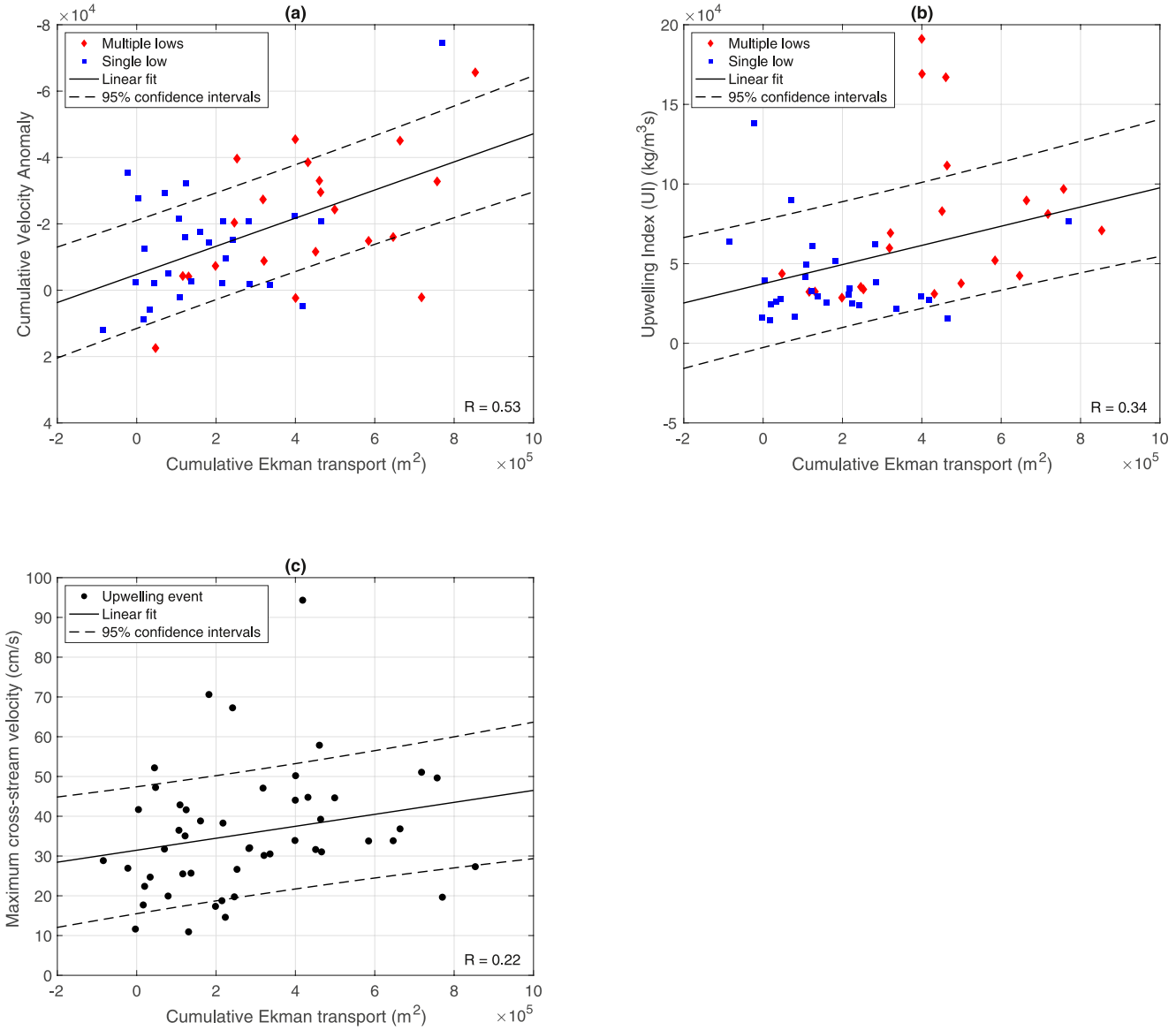

Figure 6. (a) Cumulative Ekman transport (T_{CE}) compared with cumulative velocity anomaly (CVA) for all of the upwelling events, with the linear fit and 95% confidence intervals superimposed. The events are distinguished as to whether they were associated with a single storm (blue squares) or multiple storms (red diamonds). (b) Same as (a) except for the upwelling index (UI). (c) Same as (a) except for the maximum offshore velocity in the Ekman cell (see text for details). Note that in (c) we do not distinguish between multiple low and single low events, since one representative Ekman cell is chosen for each event, regardless of the overall number of low-pressure systems that define the event.

Comparison of these variables reveals a noisy but statistically significant relationship between the strength of the forcing and the magnitude of the water column response (Figures 6a and 6b), emphasizing the fact that the upwelling diagnosed in this study is wind-driven. Not surprisingly, the type of event, single versus multiple lows, impacts the magnitude of the response. Approximately half of the upwelling events are associated with a single low-pressure system, while the other half are driven by multiple low-pressure systems. Figures 6a and 6b show that multiple low storms generally exhibit larger CVA and UI values than their single low counterparts. Note that some events exhibit positive CVA, indicating an acceleration of the WGC over the event. This is because the duration of the velocity anomaly can be significantly shorter than the duration of the density anomaly; the dynamics behind this are explained in Section 3.6.

For each upwelling event, we identified a clear cross-stream Ekman cell (see Section 3.6 for details). It is thus of interest to investigate whether the strength of the Ekman cell is correlated with the strength of the wind forcing.

To do this, we consider the maximum cross-stream velocity during each event (the onshore and offshore flow are comparable). As shown in Figure 6c, there is a significant linear correlation between the maximum cross-stream velocity and the strength of the wind forcing. According to Ekman theory, the magnitude of the cross-stream velocity is:

$$u_{ek} = {}^{\tau}/_{\rho d_{ek} f},$$

where u_{ek} is the Ekman velocity and d_{ek} is the depth of the Ekman cell (not the depth of the zero-crossing). This is consistent with the linear relationship observed between T_{CE} and the maximum cross-stream Ekman velocity (Figure 6c).

3.2.2. Composite Event

In order to characterize the general features of the upwelling, all of the events associated with a single low-pressure system (28 total) were combined to create a composite event (not surprisingly, when including the multiple storm events the composite was less-well behaved). To do so, each event in question was normalized in time onto a temporal grid ranging from 0 to 1. We then computed the spatially averaged along-coast winds, depth-averaged ocean velocity anomaly, and bottom density anomaly on this normalized grid. Given that each event is independent of the others, the signals of the normalized event are presented with standard errors.

The composite is consistent with the statistical analysis of correlations between the wind and the mooring time-series, in that the velocity weakens after the wind picks up, followed later by the presence of anomalously dense water near the bottom of the outer shelf (Figure 7). The maximum along-coast wind speed is 7 m/s out of the northwest, while the depth-averaged speed of the WGC weakens by roughly 10 cm/s. The maximum density anomaly is 0.15 kg/m^3. The vertical dashed lines in the figure denote the start and end of the event, but keep in mind that these are defined by the density signal. The average length of the events in non-normalized time is 79 $\pm$ 30 hr. By way of comparison, a similarly constructed composite of upwelling along the Beaufort Sea shelfbreak had a peak along-coast wind speed of 7 m/s and a depth-averaged velocity signal of 10 cm/s, the same as the values obtained here. However, the density anomaly in the Beaufort Sea composite was much stronger, 0.5 kg/m^3. This is because the depth of the Beaufort shelfbreak is much shallower than the west Greenland shelfbreak (50 vs. 150 m), hence more strongly stratified water is upwelled.

3.3. Hydrographic Response to Upwelling-Favorable Winds

The three shelf tripods in the OSNAP west Greenland array were designed with an additional MicroCAT situated at a depth of 50 m. The line holding these instruments was connected to the tripods with a weak link, so that they would break free if snagged by a passing iceberg (rather than dragging the tripod). Unfortunately, the common presence of icebergs in the WGCC resulted in the loss of a good number of these upper MicroCATs. Hence, it is not possible to show the mid-water column hydrographic response using the mooring data. However, in Section 3.5, we use data from a shipboard survey occupied during an upwelling event to shed light on the vertical structure of the hydrographic response.

The MicroCATs mounted directly on the tripods successfully recorded data at all three sites for all 4 yr of deployment. This permits characterization of the hydrographic response to upwelling-favorable winds at the base of the water column. For each identified storm, we define the pre-storm temperature and salinity as the average values for LS1–LS3 over the 24 hr before the onset of the density anomaly. The peak storm conditions are defined as the average over the 24 hr that bracket the maximum density anomaly during the event. As seen in Figure 8, the peak storm conditions exhibit warmer and saltier water compared to pre-storm conditions. This is consistent with upwelling of the warm, saline Atlantic-origin water in the WGC onto the shelf during the storm events. On average, the base of the water column attains a temperature and salinity of 4.1°C and 34.5, respectively, in the vicinity of the shelfbreak (Figure 8). This is 0.8°C warmer and 0.33 saltier than during pre-storm conditions. We can use the wintertime mean vertical sections of temperature and salinity across the array to deduce the depth from which this water was drawn, since most of the events occur during the winter months. This implies that upwelling events typically draw water from roughly 250 m depth and 25 km offshore of the shelfbreak. Note that while these warm, saline waters are a bit too fresh to be deemed canonical Irminger Water (Pacini et al., 2020), they nonetheless have a clear influence of this Atlantic-origin signature.

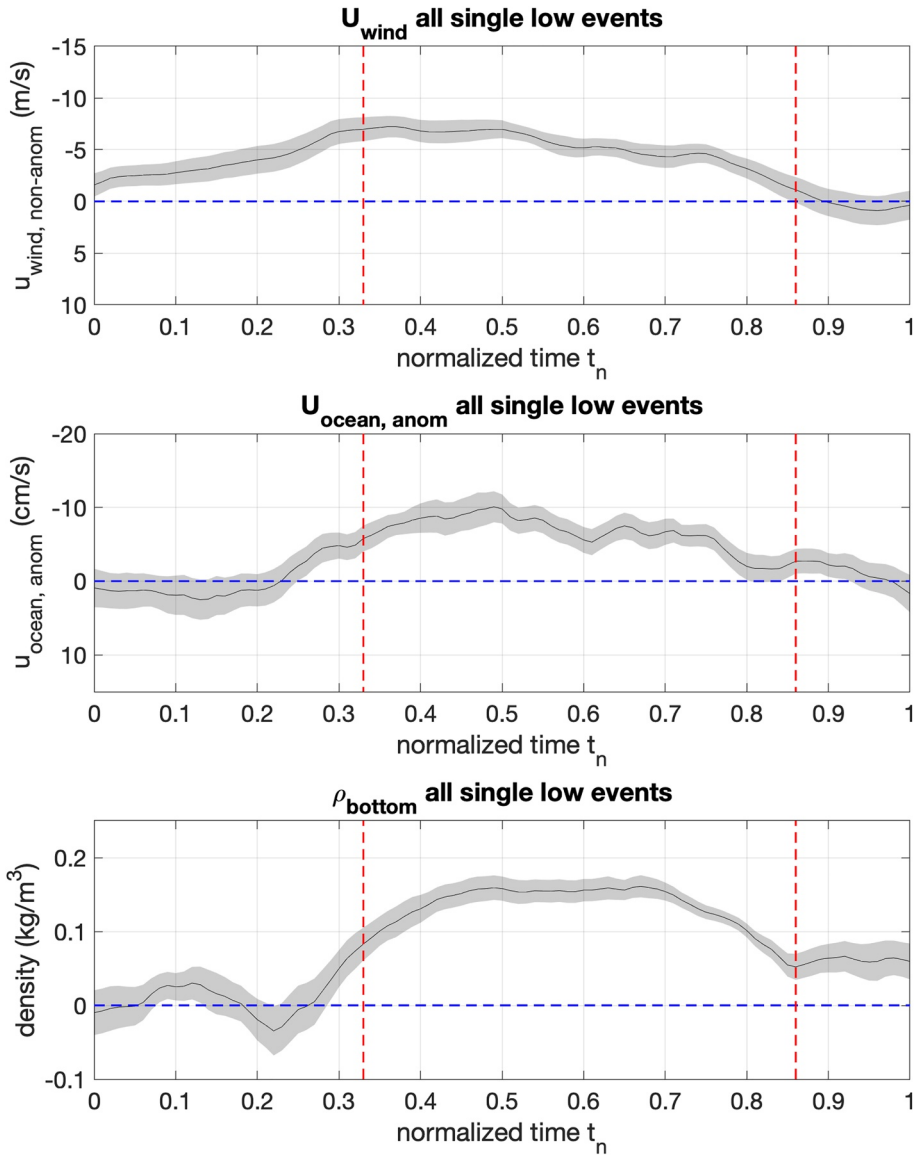

Figure 7. Composite upwelling event for the 28 single low-pressure cases, presented in normalized time over the duration of the event. The top row is along-coast wind speed, averaged over the region outlined by the white box in Figure 3a. The second row is depth-averaged velocity anomaly on the outer shelf. The third row is bottom density anomaly on the outer shelf. The shading indicates the standard error. The red dashed lines indicate the start and end times of the composite event, as defined in the text.

3.4. Nature of the Wind Forcing

As previously discussed, the winds along the west coast of Greenland are predominantly upwelling-favorable, and were consistently so during the 2014–2018 mooring deployment (Figure 3c). We thus ask: what specific wind conditions are necessary to trigger upwelling at the shelfbreak along west Greenland. Our criterion for upwelling simply stipulates that the winds must be northwesterly for a portion of the event, but it is of interest to examine the strength of the winds in relation to the low-pressure signatures, in order to understand the atmospheric dynamics that are responsible for the upwelling.

To do this, we examine the 3-hourly maps of SLP and 10 m winds during the upwelling events. Detailed inspection of each individual event reveals that upwelling is driven by synoptic-scale low-pressure systems that enter the region along the North Atlantic storm track and enhance the northwesterly winds along west Greenland. The shorter upwelling events correspond to only one low-pressure system, while the longer events are the result of a train of cyclones that do not allow the density signature to relax back to pre-event conditions (see Section 3.2). Of

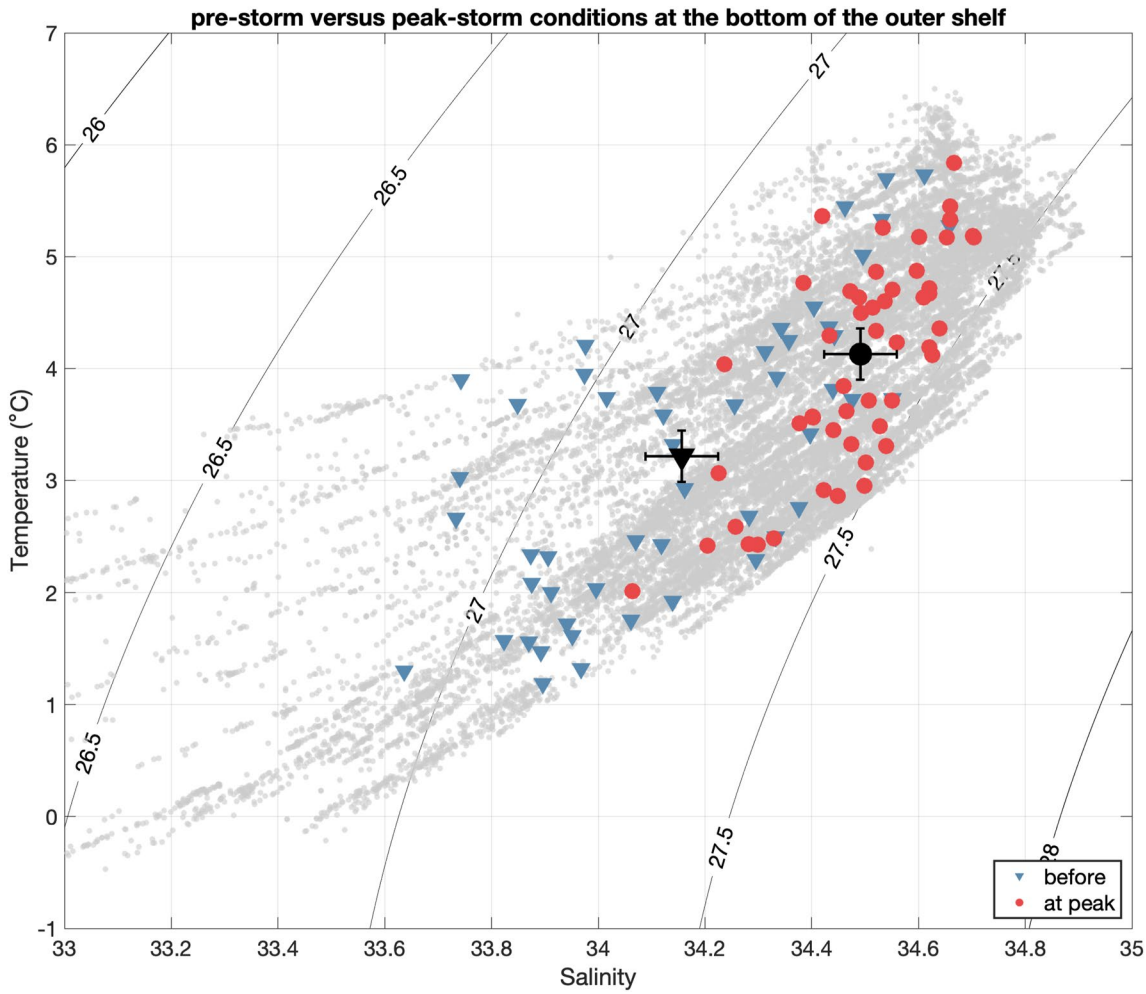

Figure 8. Mean hydrographic properties for the 24 hr before an upwelling event (blue triangles) and during the 24 hr surrounding the peak of each upwelling event (red circles) averaged at the base of the shelf (tripods LS1–LS3). The overall mean values prior to and during the storm are shown by the black symbols, where the error bars represent the standard error. The gray dots indicate all of the hydrographic measurements from the MicroCATs at LS1–LS3 during the 49 upwelling events.

the 49 upwelling events, 28 were due to one low-pressure system, while the remaining 21 were driven by between 2 and 9 distinct low-pressure systems. Notably, 16 of the events ended with a transition to downwelling conditions induced by strong southeasterly winds. These winds are also the result of low-pressure systems progressing along the storm track, but, in this scenario, the low has impinged on Cape Farewell farther to the northwest and thus the strong southeasterlies on the eastern end of the low act to reverse the density anomaly. Future work will address the downwelling that occurs along the west Greenland shelfbreak.

To diagnose the atmospheric conditions during upwelling, we created composite SLP and 10 m wind fields at 12 hr intervals surrounding the event, where the peak storm period is defined as the timestep at which the winds reach their maximum value. The composite of all 49 upwelling events during peak conditions reveals a strengthened Icelandic low relative to the mean state (compare Figure 9a with Figure 3a; note the different colorbars). Associated with this deep low is a region of high (>15 m/s) northwesterly wind extending from the west coast of Greenland to southeast of Cape Farewell (Figure 9b). This wind pattern is strikingly reminiscent of a forward tip jet. Inspection of the full set of composites (not shown) reveals that the peak upwelling along west Greenland in fact occurs as a tip jet is first developing. This is consistent with Våge et al. (2008, 2009), who presented the evolution of forward tip jets using composite maps. In both of these studies, the composite winds 12 hr prior to peak tip jet conditions southeast of Cape Farewell resemble the conditions seen in Figure 9 during peak upwelling.

Are all upwelling events the result of forward tip jets? We can answer this by applying the method used by Våge et al. (2008) to objectively define forward tip jet events. In particular, Våge et al. (2008) used the zonal wind

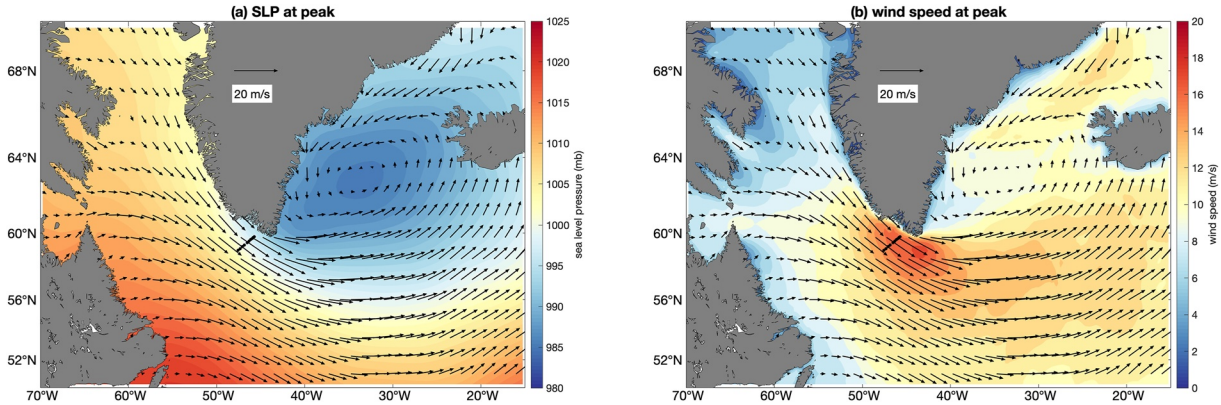

Figure 9. (a) Composite sea level pressure (SLP; color) and 10 m wind vectors during peak upwelling for all 49 events. Every fifth velocity vector is plotted. The black circles denote the moorings of the Overturning in the Subpolar North Atlantic Program west Greenland array. (b) Same as (a) except for wind speed (color), with the wind vectors superimposed.

speed, SLP gradient, and air temperature in the vicinity of Cape Farewell in an empirical orthogonal function calculation. Strong forward tip jets are defined as those where the reconstructed zonal wind speeds are in excess of 25 m/s. We note that Våge et al. (2008) used scatterometer wind data in their analysis, which typically exhibit stronger speeds in this region than reanalysis products do (e.g., Moore & Renfrew, 2005; Våge et al., 2008). For the ERA5 reanalysis data used here, we use a seasonally varying threshold of 10 m/s for fall/winter/spring, and 5 m/s for summer (results are not sensitive to these exact threshold choices). These reduced wind speed thresholds as compared to those of Våge et al. (2008) ensure that all tip jets, not just strong tip jets, are identified. This revealed that all but one of the upwelling events corresponded to an early stage tip jet (the exception was an upwelling event in August 2017 when the low-pressure center that induced upwelling favorable winds was too far southeast of Cape Farewell to be considered a tip jet). This places even more importance on these small-scale features, which, in their fully developed stage, strongly influence conditions in the Irminger Sea, including LSW formation and downwelling along the east coast of Greenland. As shown below in Section 3.5, this downwelling in fact plays a role in the evolution of the upwelling events considered here.

3.5. Case Studies of Two September Storms

We now present two case studies to shed light on the vertical redistribution of properties due to upwelling-favorable winds. The first is an upwelling event in September 2014 described using the mooring timeseries, and the second is an upwelling event in September 2018 described using shipboard data. The two studies offer complimentary views since the former has high temporal resolution, while the latter has high spatial resolution.

3.5.1. 2014 Storm

This event lasted from 14–18 September 2014. The three diagnostic timeseries defined in Section 3.1 are shown in Figure 10 (we have included the 48 hr segment before the onset of upwelling). During the event, the wind peaked at 15 m/s, the depth-averaged along-stream velocity decreased by 30 cm/s, and the bottom density anomaly reached 0.12 kg/m^3 (the corresponding values from the composite event of Figure 7 are 7 m/s, 10 cm/s, and 0.15 kg/m^3, respectively). The event ended due to the arrival of a downwelling-favorable low-pressure system. This can be seen in the zero-crossing of the along-coast winds on 16 September, which ultimately causes the density anomaly to return to zero about 1.5 days later.

Three 12 hr periods during the event are shown to highlight important features and the development of the water column response. Period 1 represents pre-storm conditions, period 2 represents peak storm conditions, and period 3 represents end of storm conditions (see the gray bars in Figure 10). Prior to the storm, the along-coast winds are weakly positive (southeasterly; Figure 10). At this point, the low-pressure system that will ultimately result in the upwelling is situated off the Canadian landmass with a central pressure of ~990 mb (Figure 11a). The along-stream velocity is approximately 30 cm/s (Figure 11b), and the cross-stream velocity is weak (Figure 11c), both of which are representative of the mean flow conditions (Pacini et al., 2020).

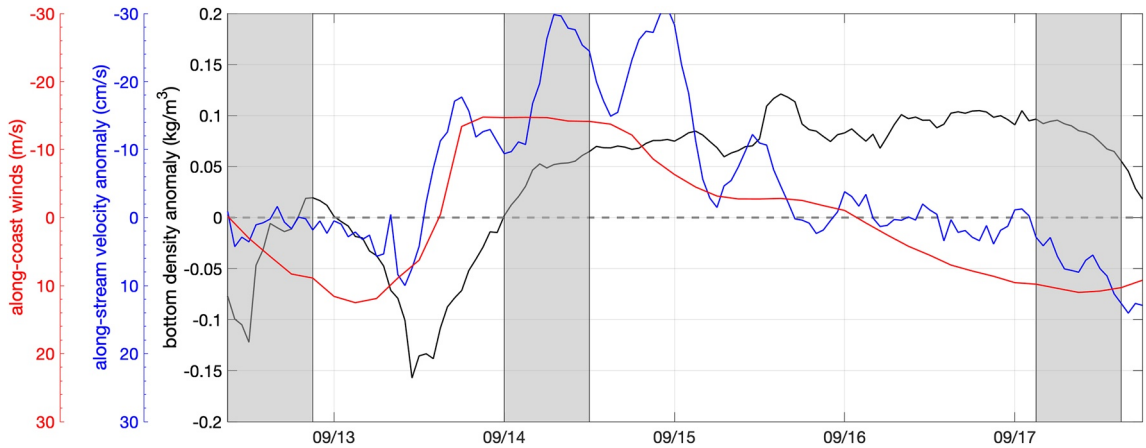

Figure 10. Timeseries of along-coast winds (red) averaged in the white box shown in Figure 3a, along-stream velocity anomaly on the shelf (blue), and bottom density anomaly on the shelf (black) for an upwelling event in September 2014. The gray bars mark the periods of the three composites shown in Figure 11.

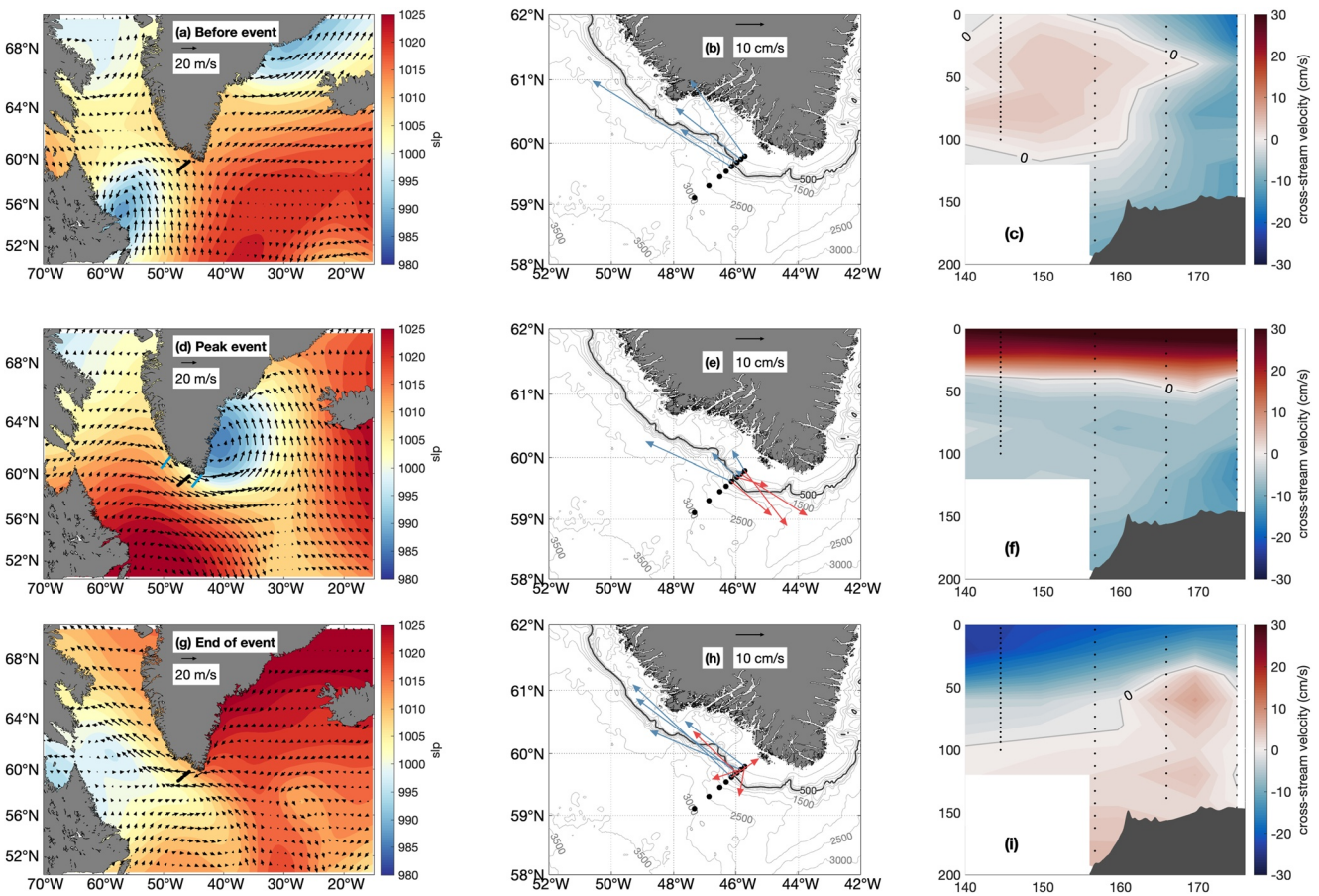

Figure 11. Evolution of the September 2014 upwelling event. Top row: pre-event conditions (averaged over the 12 hr represented by the first gray bar in the figure). Middle row: peak-event conditions (middle gray bar in the figure). Bottom row: end of event conditions (last gray bar in the figure). (a, d, g) Sea level pressure (SLP; color) and wind vectors. The black symbols are the Overturning in the Subpolar North Atlantic Program west Greenland moorings, and the blue lines in (d) denote the boundaries of the high wind speed region used for the flux calculations of Section 3.6. (b, e, h) Depth-averaged velocity vectors (blue) and velocity anomaly vectors (red), where the anomalies are relative to the velocity vectors in (b). (c, f, i) Vertical section of cross-stream velocity (color) with the zero value contoured. The black dots are the acoustic Doppler current profiler data points.

Approximately 48 hr later, at the peak of the storm, the low-pressure system is now in the lee of Greenland in the Irminger Sea, with a central pressure of 986 mb, causing strong northwesterly winds at Cape Farewell and along west Greenland (Figure 11d). The along-stream flow is significantly reduced (note the anomaly vectors indicating a reduction of 20 cm/s, where the anomaly is computed relative to the pre-storm conditions; Figure 11e). During this particular event, the winds were strong enough to reverse the flow at LS2 for 12 hr. Notably, there is now a clear presence of an Ekman cell, with strong offshore flow (~30 cm/s) in the top 40 m and weaker, bottom-intensified onshore flow beneath this (Figure 11f). Such an Ekman cell was evident in all of the events.

The vertical structure of this secondary circulation can be characterized as a function of bottom slope and hydrography of the water column. Specifically, Lentz and Chapman (2004) demonstrate that the deep return flow during upwelling is either spread over a significant portion of the water column or confined to a bottom boundary layer, in which case the surface and bottom stress balance each other. To quantify this, we computed the slope Burger number, $B = \alpha N/f$, where α is the bottom slope and N is the stratification (calculated from the hydrographic sections presented in Section 3.5). When B is O(1) or greater, the return flow at depth is expected to extend vertically above the bottom boundary layer. By contrast, when $B \ll 1$, the return flow is confined to the bottom boundary layer. We find that B is ~0.1 throughout the shelf, indicating that the return flow should be confined to the bottom boundary layer. This bottom-intensification is consistent with the composite in Figure 11f. This result is in contrast to the upwelling across the Beaufort Sea shelfbreak investigated by Pickart et al. (2013). In that case, B was O(1) due to the stronger stratification (associated with the shallower shelfbreak), and the return flow extended above the bottom boundary layer.

In the final period, associated with ramp-down conditions, the parent low has completely filled, and a second low has developed in the vicinity of Hudson Strait. This causes strong southeasterly winds along the west coast of Greenland (Figure 11g). While the along-stream flow in the vicinity of the shelfbreak has been re-established (Figure 11h), the cross-stream flow does not return to the weakened values indicative of the start of the event. Rather, there is now a reverse Ekman cell, triggered by the downwelling-favorable winds (Figure 11i).

3.5.2. 2018 Storm

As noted above, due to the presence of icebergs in the region, we were unable to consistently maintain MicroCATs above the shelf tripods. Hence, it is not possible to describe the evolution of hydrographic properties higher in the water column during storm events using the mooring data. However, high-resolution hydrographic shipboard surveys are carried out when the mooring array is serviced, and, during the 2018 cruise, the OSNAP west Greenland mooring line was occupied twice with closely spaced CTD stations (~3.5 km station spacing). Since none of the tripods were deployed during this time period (they were being refurbished on the ship), we can not use the same criteria for defining upwelling events as was applied to the mooring data. However, the ERA5 wind data indicate that the first CTD section was occupied shortly after the along-coast winds became strong enough to induce upwelling, while the second section was done as the upwelling winds subsided. Hence, these can be considered ramp-up and ramp-down conditions (Figure 12a).

The vertical sections of temperature and salinity for both crossings are shown in Figures 12b–12e. The hydrographic conditions during the ramp-up period reflect canonical conditions at the shelfbreak and on the shelf, where warm, saline waters reside offshore and a cold, fresh wedge is present between the surface and inshore-most point on the line. A few days later, the hydrographic properties were re-arranged: the cold, fresh wedge was shifted offshore at the surface, while the warmer, more saline water was found on the outer shelf in the lower part of the water column. This redistribution of properties is highlighted in the anomaly sections (Figures 12f and 12g). This change in properties is consistent with the presence of an Ekman cell during upwelling conditions where the surface waters are advected offshore and waters at depth are advected onshore. Additionally, the magnitudes of these hydrographic anomalies (~1°C in temperature and ~0.3 in salinity) are consistent with the results of Section 3.3 where, on average, the near-bottom water was 0.8°C warmer and 0.33 saltier during peak storm conditions as compared to pre-storm conditions.

3.6. Cross-Stream Property Fluxes

It is of interest to quantify the cross-stream fluxes of freshwater and heat during upwelling, in order to create property budgets and assess the implications for both the interior Labrador Sea and the west Greenland shelf. Using our mooring timeseries together with the shipboard CTD data, we now estimate the net freshwater and heat

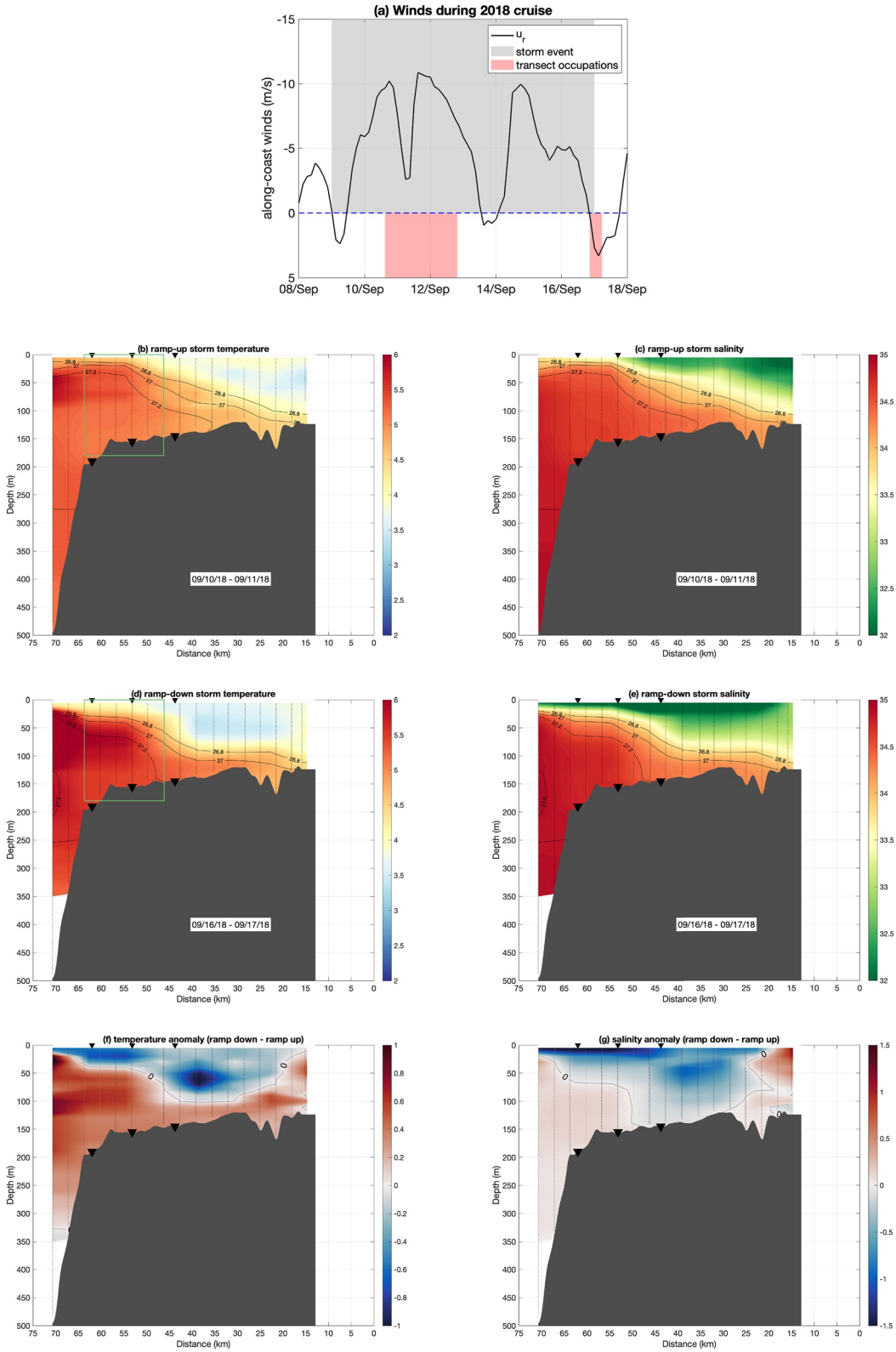

Figure 12.

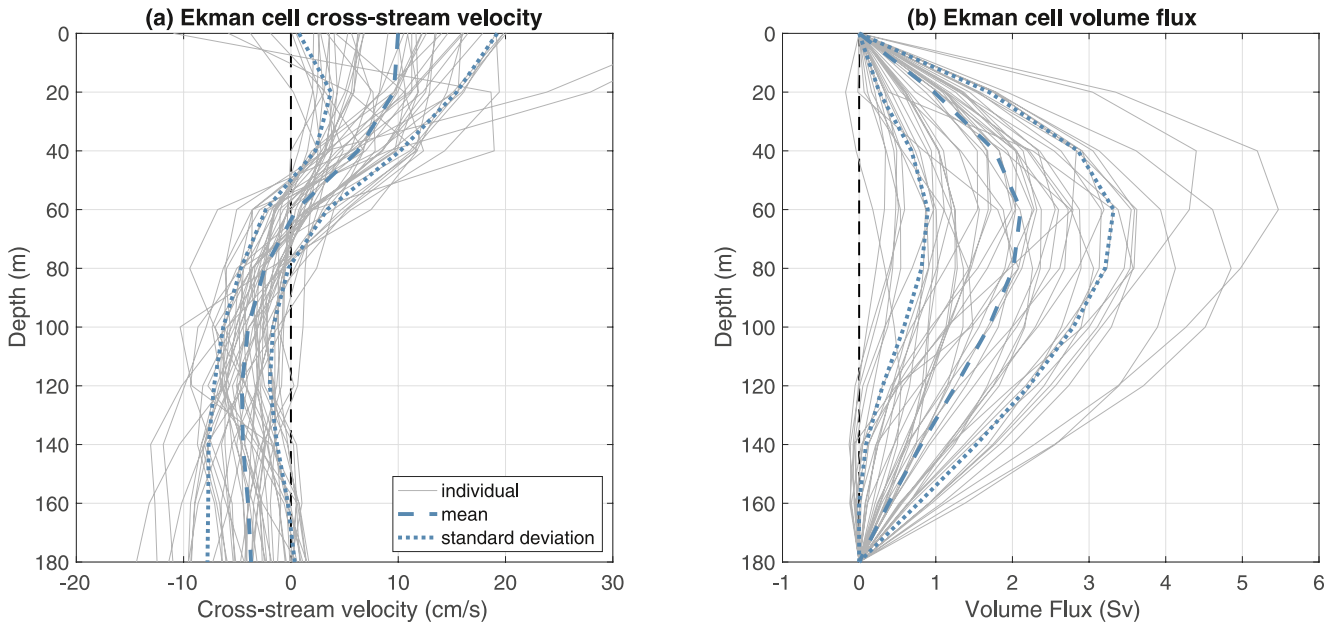

Figure 13. (a) Vertical profiles of cross-stream velocity on the shelf averaged over the time period that the Ekman cell was present for each upwelling event (gray lines). The overall mean vertical profile is dashed blue, with the standard deviation envelope denoted by the dotted lines. (b) Same as (a) except for depth-integrated Ekman cell volume flux.

flux associated with each upwelling event. In order to do this, we need to combine information from the two data sources presented in the previous section: high-resolution temporal data from the moorings and high-resolution hydrographic data from the shipboard surveys.

Using the mooring record, we identified the period of Ekman cell existence during each of the 49 upwelling events. We then computed a mean vertical profile of cross-stream velocity averaged over this time period and averaged spatially over the vicinity of the shelfbreak (the domain of Figure 2, green box) for each event. These vertical profiles of cross-stream velocity are shown in Figure 13a (gray lines), indicating offshore velocity in the upper 50 m, and onshore velocity at depth.

For each vertical profile of cross-stream velocity, the volume flux per unit depth was computed for the segment of the west Greenland shelf subject to the upwelling winds (approximately 500 km long, see Figure 11d). For a balanced Ekman cell, the vertical integral of this curve should be zero. This was nearly so for each profile, but, realizing that the data are not perfect, a small barotropic offset was applied throughout the water column to adjust the profile to exactly balance mass (Figure 13b). On average, this offset was 3.3 cm/s. An analogous offset was used by Pickart et al. (2013) in their flux calculations for an upwelling event along the Beaufort slope. As seen in Figure 13b, the average amplitude of the Ekman cell is 2 Sv, but individual events can range in intensity from near-zero volume flux to greater than 5 Sv.

A consequence of this balanced-mass profile is that we can compute heat and freshwater fluxes that are insensitive to the reference temperature or salinity. This is formally true for the heat flux, and empirically the case for salinity. Even though the reference salinity appears in the denominator of the freshwater flux equation, changing this value has a negligible impact on the net freshwater flux. This was demonstrated by conducting sensitivity tests using a range of reference salinities from 34 to 36, which only changed the net freshwater flux by 13.8 mSv, or 5% of the overall flux. By contrast, for a velocity profile that is unidirectional (i.e., does not balance mass), the

Figure 12. (a) Timeseries of along-coast winds averaged within the white box in Figure 3a from 8 September to 18 September during the 2018 OSNAP cruise. The gray shading indicates the upwelling event, and the red shading indicates the time period of the two conductivity-temperature-depth (CTD) sections. (b) Temperature (color, °C) during the first occupation, overlain by density (contours, kg/m^3). The black triangles indicate the locations of the LS1–LS3 tripods, and the thin vertical lines denote the CTD casts. The *x*-axis is distance offshore, with 0 km corresponding to the coast. The green boxes in (b and d) indicate the regions used for calculation of the hydrographic profile during the storm event used in Section 3.6. (c) Salinity (color) during the first occupation, overlain by density (contours). (d) Same as (b) except for the second occupation. (e) Same as (c) except for the second occupation. (f) Difference in temperature between the second and first occupations of the line (the zero value is contoured). (g) Same as (f) except for salinity.

net freshwater flux changed by 3,000% over this range of reference salinities. We note that a similar sensitivity test for the heat flux resulted in comparably small changes in the flux for a balanced velocity profile, even though the heat flux is formally insensitive to the reference temperature. This suggests that, in both cases (heat flux and freshwater flux), the small sensitivity is due primarily to numerical integration error. The results presented below for the freshwater flux are computed using a reference salinity of 35, but we stress that this is an arbitrary choice that does not impact the results.

To compute heat and freshwater fluxes, we need high-resolution vertical profiles of temperature and salinity. As explained in Section 3.3, the mooring data are too sparse to provide this information. Thus, we use shipboard CTD data to derive these profiles. Specifically, we construct average profiles of temperature and salinity on the west Greenland shelf in fall using data from the 2018 OSNAP survey, and in winter using data from the 1997 R/V *Knorr* survey (see Section 2.3 for details). Comparison with the bottom MicroCAT records on the shelf indicate that these profiles are representative of seasonal conditions at the base of the water column during their respective periods. Since the subsequent analysis takes place over the fall and winter season, we average these fall and winter profiles together to obtain the hydrographic profiles required for the flux calculations.

The resulting heat flux per unit depth and freshwater flux per unit depth are shown in Figures 14b and 14c. These curves were then vertically integrated to obtain the absolute heat and freshwater fluxes. As expected, there is a net onshore transport of heat and offshore transport of freshwater. On average, the Ekman cell is present for 21 hr for a given storm (Section 3.6). Recall, however, that 21 of the 49 events correspond to multiple low-pressure systems. This results in an average of 2.6 storms per event, where each low-pressure system causes a distinct Ekman cell. Hence, to obtain the net transfer of properties for a representative upwelling event we integrate the fluxes over a period of 54 hr (21 × 2.6).

This results in a total of 414 km^3 of water exchanged across the shelfbreak per upwelling event, with 1.88×10^{18} J of heat fluxed onshore and 13.5 km^3 of freshwater fluxed offshore. To provide context, the volume of water exchanged by a single storm represents 9% of the total volume of the west Greenland shelf subject to the wind forcing. Hence it would take 11 such storms to completely flush this portion of the shelf. Since there are on average 12 upwelling events per year, this implies that the entire shelf is replenished each year due to upwelling.

We note that it is not assumed that the water being advected onshore in the bottom Ekman layer is transformed into the water being advected offshore in the surface Ekman layer. Rather, the upwelling event is a three-dimensional scenario in which the freshwater being fluxed offshore originated predominantly from upstream in the WGC. That said, the onshore/offshore flux across the shelfbreak is computed as a section flux, not as part of a three-dimensional volume budget calculation. An analogs scenario in the Beaufort Shelfbreak Current was analyzed by Pickart et al. (2011) using a combination of mooring observations and a regional numerical model. The model Lagrangian trajectories indicate that the water fluxed offshore in the surface Ekman layer during the storm mostly came from upstream in the boundary current.

3.6.1. Upstream Impact on the Cross-Stream Fluxes

The Ekman cell associated with the September 2014 storm event described above persisted for only 12 hr (the length of time over which the composite of Figure 11f was computed), even though the actual event duration, as defined by the density anomaly, was approximately 72 hr. Inspection of all of the single-storm events reveals that, on average, the Ekman cell lasts 21 ± 2.1 hr, while the along-stream velocity signal lasts 11.3 ± 2.5 hr. This is in contrast to the average length of the events, based on the density signal, of 79 ± 5.6 hr, as well as the average length of the wind forcing which is 77 ± 6.7 hr. What causes the shutdown of the velocity response prior to the relaxation of the local storm winds? This is of importance because it impacts the magnitude of cross-shelf fluxes: the longer the persistence of the Ekman cell, the more water is exchanged across the shelfbreak.

Because of the pronounced change in coastline orientation on either side of Cape Farewell, the low-pressure systems in the Irminger Sea that drive forward tip jets and upwelling-favorable winds along west Greenland also result in downwelling conditions along east Greenland (see Figure 9). Numerous studies have investigated the propagation of coastal trapped waves along the east coast of Greenland in response to such barrier winds (Gelderloos et al., 2021;Harden, Renfrew, et al., 2014; Harden, Straneo, et al., 2014; Le Bras et al., 2018; Pacini et al., 2020). Following Brink (1982), we calculate the barotropic phase speed of the coastal trapped wave as $c_o = {}^{fL(H-h_s)}/_{H}$, where H is the basin depth, h_s is the shelf depth, and L is the width of the shelf. This gives a value of roughly 3.5 m/s, which is the speed at which the velocity response to wind intensification (the SSH anomaly) would travel along east Greenland, and the speed at which this signal would round Cape Farewell. We note that the arrival of the barotropic

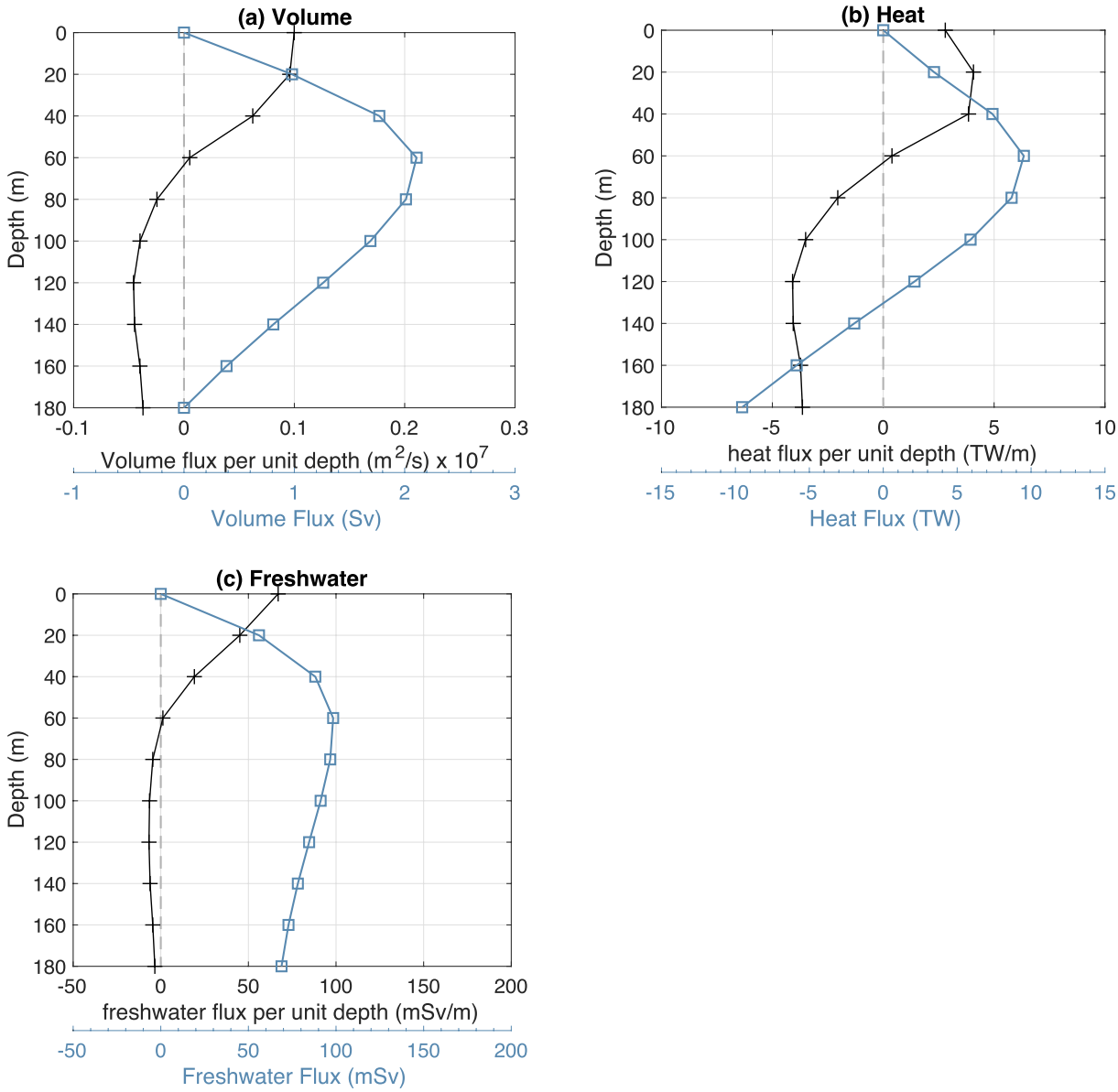

Figure 14. (a) Volume flux per unit depth (black curve) and depth-integrated volume flux (blue curve) for the average upwelling event. (b) Heat flux per unit depth (black curve) and depth-integrated heat flux (blue curve). (c) Same as (b) except for freshwater.

wave should be considered the arrival of a front due to the continual sea surface displacement upstream, as derived in Allen (1976). This is also evident in the modeling results of Pickart et al. (2011), where a barotropic coastal trapped wave on the Beaufort shelfbreak, trigged by upwelling, is shown to propagate as a front (see their Figure 18d).

The distance between the northeast side of Cape Farewell and the OSNAP west Greenland mooring array is ~200 km. A barotropic wave traveling this distance would thus take ~16 hr to propagate from Cape Farewell to the OSNAP west Greenland mooring array. Recall that wind conditions along west Greenland lead wind conditions along east Greenland by 3 hr. We can therefore assume that the downwelling signal along east Greenland induced by a developing forward Greenland tip jet will be initiated 3 hr after the start of upwelling conditions along west Greenland. Accounting for this lag time, we obtain a wave propagation timescale of 19 hr, which is very close to the average shutdown timescale for the upwelling velocity response at the array (keep in mind that there is uncertainty in the wave speed).

Is the magnitude of the velocity anomaly introduced by the coastal trapped wave large enough to shut-down the along-stream velocity anomaly and Ekman cell along west Greenland? In order to quantify the impact of

downwelling-favorable winds on the sea level along east Greenland, and ultimately on the along-stream velocity along west Greenland, we compute

$$\eta = \int_0^x {}^{\tau^x}/_{\rho_0 g H}\, dx$$

following Sofianos and Johns (2001), where η is the sea level height, τ^x is the along-coast wind stress, H is the depth of the of the Ekman layer (taken to be 40 m based on the results presented in Section 3.5), and ρ_o is the density (1,026.8 kg/m^3). We compute τ^x by (a) rotating the wind vectors into along-coast and cross-coast components (using 18°T) along east Greenland; (b) identifying the time step where downwelling is initiated along east Greenland for each upwelling event along west Greenland; (c) extracting the wind stress from a box along east Greenland defined by 60°–61°N and 41°–43°W; and (d) taking a latitudinal average of wind stress throughout this domain. We then integrate zonally across the domain to obtain η for each upwelling event. We find that $\eta = 2.0 \pm 1.5$ cm, consistent with the model results of Gelderloos et al. (2021), who compute sea level anomalies induced by coastal trapped waves on the Greenland shelf of the same magnitude. Through geostrophy, the impact of this sea level anomaly on the along-stream flow is computed to be 2.7 ± 2.1 cm/s.

Recall that along-stream velocity anomalies at the array site reach a maximum of 10 cm/s 6–9 hr after the wind increases. However, as explained above, the coastal trapped wave does not reach west Greenland for 19 hr. Thus, the along-stream velocity relaxes for the intervening 10 hr between maximum flow and the arrival of the coastal trapped wave, from 10 to ∼5 cm/s (see Figure 7). This along-stream velocity anomaly is comparable in magnitude (within the error bars) to the above computed coastal trapped wave signal.

These results suggest that the Ekman cell and the along-stream flow signature are prematurely shut off due to the orientation of the Greenland coastline and the propagation of the downwelling signal from upstream. This mechanism for Ekman cell shutdown is similar to the results presented in A. J. Clarke (1977), where a storm that induces upwelling-favorable conditions on one side of Lake Ontario also induces downwelling-favorable conditions on the other side of Lake Ontario. From meteorological buoys and coastal current meter arrays, A. J. Clarke (1977) demonstrated that when the downwelling signature from upstream propagates around the basin at the coastal trapped wave speed, it adjusts the pycnocline from upwelling conditions (pycnocline displaced upwards) to downwelling conditions (pycnocline displaced downwards) and prematurely shuts down the upwelling signature.

3.7. Impact on Convection in the Basin

Given the offshore flux of freshwater due to the regular occurrence of upwelling along the southwest Greenland coast, we now seek to quantify the impact that this has on the wintertime development of the mixed layer and the production of newly ventilated LSW. Deep convection regularly occurs in the western portion of the Labrador Basin (e.g., R. A. Clarke & Gascard, 1983; Pickart et al., 2002; Yashayaev & Loder, 2016), and has also been observed in the region south of Cape Farewell (Piron et al., 2017; Zunino et al., 2020). By contrast, wintertime mixed layers in the eastern Labrador basin are generally shallower (less than 800 m; Lavender et al., 2002; Piron et al., 2017; Zunino et al., 2020). There is, however, no a priori reason why this should be the case: the buoyancy forcing is just as strong (or stronger) in the eastern basin as it is south of Cape Farewell (Pickart et al., 2002). Furthermore, there is a local cyclonic recirculation situated over the deep continental slope of west Greenland, extending from approximately Cape Farewell to Cape Desolation (Figure 4a; Lavender et al., 2000), which is associated with domed isopycnals. Hence, both the buoyancy forcing and the hydrographic preconditioning are conducive for deep convection (Marshall & Schott, 1999).

We suspect that the freshwater fluxed off the boundary due to the regularly occurring upwelling storms acts to inhibit the mixed layer depths (MLDs) in the vicinity of the recirculation gyre. This notion is consistent with the model results of Schulze Chretien and Frajka-Williams (2018) in which wind forcing is the predominant mechanism for surface particles to be fluxed offshore from the west Greenland shelf. In particular, water parcels in the model are able to be transported roughly 50 km offshore of the 2,500 m isobath, which is far enough to penetrate the recirculation gyre.

To investigate this, we invoked the one-dimensional mixed layer model (PWP, see Section 2.5). To obtain an initial fall profile of temperature and salinity, we averaged together all Argo data within the region of the recirculation gyre from November 2014 (see Section 2.4 and Figure 4 for details). The resulting mean profiles (blue curves in Figures 4d and 4e) display a warm, fresh surface layer extending to roughly 50 m, beneath which lies the Irminger Water from roughly 100–600 m. This is the remnant warm, salty Atlantic-origin water that has been transported cyclonically around the subpolar gyre.

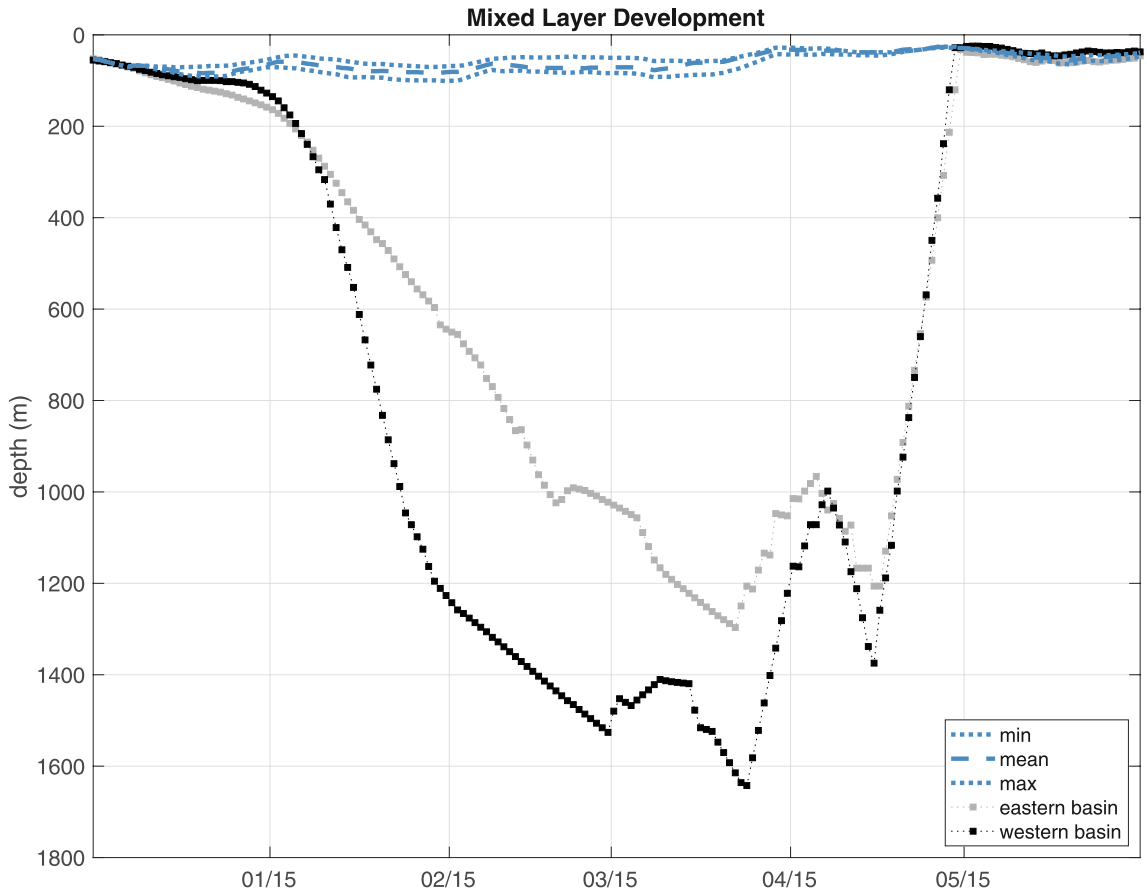

Figure 15. Fourteen-day running mean mixed layer depth development over the 2014–2015 winter convective season using PWP. Five cases are shown: the western basin run (black); the control run for the recirculation gyre of the southeastern Labrador Sea (gray); and three freshwater flux runs using the mean volume flux profile in Figure 13a (blue dashed line), as well as the one standard deviation envelope of this profile (blue dotted lines).

The model was forced with daily ERA5 heat flux and wind velocity timeseries for the winter of 2014–2015, spatially averaged within the same domain (57°–59.5°N and 52°–55°W for the western region; 57.6°–59.5°N and 45°–49.5°W for the eastern region). P-E was neglected as it has very little impact (e.g., Lazier et al., 2002; Pennelly & Myers, 2021). We begin with a control run in which there is no source of freshwater emanating from the boundary. Figure 15 (gray curve) shows the evolution of the MLD from late-fall to late-spring (low-passed using a 14-day running mean in order to reduce the noise in MLD). The mixed layer progressively deepens beginning in December until it reaches its maximum depth of ∼1,300 m in early March. Following this, the MLD rapidly decreases, and the water column completely re-stratifies by early May. (Excursions from this seasonal deepening/shoaling of the mixed layer over the course of the PWP run are due to variations in the air-sea forcing during this particular winter.)

For comparison, we did a second run without freshwater forcing corresponding to the western Labrador Basin (with the initial hydrographic profiles and air-sea forcing appropriate for that region). In this case, the MLD extends approximately 300 m deeper to a depth of ∼1,600 m (Figure 15, black curve). This deepening occurred almost 2 weeks sooner than in the eastern basin. Encouragingly, the results of this second PWP run compare well with the MLD observations of Yashayaev and Loder (2016) for winter of 2015, which showed maximum convective depths of 1,500 m in the interior Labrador Sea. This gives us confidence in the fidelity of our PWP simulations.

To assess the impact of the freshwater flux from upwelling events on the development of the MLD in the eastern basin, we carried out the following exercise. Recall that there were 49 upwelling events over the 4 yr study period. Of these, 39 events occurred during the months of November–May, implying 10 events per winter. Using the cross-stream flux results from Section 3.6 for a single storm, this amount of freshwater was injected evenly throughout the top 40 m at 10 regularly spaced intervals over the winter season. In particular, we injected 0.31 m of freshwater (13.5 km^3 divided by the area of the recirculation gyre, 4.47×10^4 km^2) for each event. A

distribution depth of 40 m was chosen since this is the average depth of the upper branch of the observed Ekman cells (see Section 3.5). Similarly, we applied a temperature anomaly of −0.10°C distributed over the top 40 m for each of the 10 events since the freshwater is anomalously cold. This value was obtained using the density and heat capacity of water and was applied over the same area and depth layer as the freshwater flux calculation. However, this did not have a significant effect on the development of the mixed layer.

We realize that the exact area over which the freshwater is spread is subjective. This choice is guided by various modeling studies that address the penetration of freshwater off the west Greenland shelf (e.g., Schulze Chretien & Frajka-Williams, 2018). This water would preferentially become trapped within the recirculation gyre just offshore of the west Greenland slope, due to the closed contours of absolute dynamic topography (see Figure 4a). Hence, choosing this area for both the initial eastern Labrador Sea profile and lateral region over which to spread the freshwater is a reasonable assumption. We also recognize that the following results provide an upper bound for the freshwater emanating from the boundary current, as we have not included periods of downwelling. We do not consider downwelling scenarios because it is unknown from how far offshore the freshwater fluxed onshore will emanate. This is the focus of future work.

As seen in Figure 15 (blue dashed curve), this addition of freshwater has a marked effect on the depth of convection. The mixed layer development is much slower, and the deepest MLD is only 100 m. This result is in line with the relatively shallow MLD observations within the recirculation gyre (e.g., Piron et al., 2017; Zunino et al., 2020). Our analysis thus implies that the repeated occurrence of wind-driven upwelling along the west coast of Greenland prohibits deep convection from occurring in the southeastern Labrador Sea. Error bounds on this MLD timeseries are calculated by considering the freshwater flux and heat flux induced by the one standard deviation envelope around the mean volume flux profile in Figure 13b. As shown in Figure 15, the MLD is approximately 50 m deeper when the minimum volume flux profile is used, and is approximately 50 m shallower when the maximum volume flux profile is used. This highlights the robustness of our result.

4. Conclusions

Using data from the OSNAP west Greenland mooring array, 49 upwelling events were identified over the 4 yr period 2014–2018. The events are characterized by intensified northwesterly winds, a reduction in the along-stream velocity in the vicinity of the shelfbreak, and a positive density anomaly at the base of the outer shelf. The secondary circulation present during the upwelling fluxes cold, fresh meltwater offshore at the surface and warm, saline Atlantic-origin water onshore at depth. On average, the upwelling events warm the base of the shelf by ∼0.8°C and increase the salinity by ∼0.33.

This redistribution of hydrographic properties was shown to have a substantial impact on the development of the mixed layer in the interior Labrador Sea. Using a one-dimensional mixed layer model, we demonstrated that the freshwater flux can delay the onset, and reduce the overall depth, of deep convection in the interior Labrador Sea. This synoptic-scale freshwater source therefore provides an explanation for why deep mixed layers are not observed in the southeastern Labrador Sea. As such, models need to account for this small-scale variability in order to accurately reproduce wintertime production of LSW.

The upwelling events occur during the development stage of a forward Greenland tip jet, a common atmospheric phenomenon in the vicinity of Cape Farewell during the winter season. While previously shown to impact LSW production in the Irminger Sea (e.g., Pickart, Spall, et al., 2003; Pickart, Straneo, et al., 2003; Våge et al., 2008), our study reveals that forward tip jets also impact LSW formation in the Labrador Sea. While they enhance LSW production in the southwestern Irminger Sea, they reduce LSW production in the southeastern Labrador Sea.

Data Availability Statement

All data from the OSNAP WG array can be found at www.o-snap.org. The 2014–2016 mooring data are located at https://doi.org/10.7924/r4fj2dr7k (Pickart, 2018), and the 2016–2018 mooring data are located at https://doi.org/10.35090/fz80-6c32 (Pickart, 2020). The 2018 shipboard survey data can be found at https://doi.org/10.35090/gatech/66765 (Pickart, 2022), and the 1997 shipboard survey data can be found at https://cchdo.ucsd.edu/cruise/316N147_5 (Pickart, 2021). The Argo data can be found at the Scripps Institution of Oceanography Argo platform (https://argo.ucsd.edu/data/) (Argo, 2021). The ERA5 data are available on the ECMWF server at: https://www.ecmwf.int/en/forecasts/datasets/reanalysis-datasets/era5 (Hersbach et al., 2018).

Acknowledgments
The authors thank John Kemp, Jim Ryder, Brian Hogue, Andrew Davies, and Rick Trask for the design, fabrication, and deployment of the mooring array. The authors also acknowledge the captain and crew of the R/V *Knorr* and R/V *Neil Armstrong* for the successful recovery and deployment cruises. Funding for the study was provided by National Science Foundation Grants OCE-1259618 and OCE-1756361.

References

Allen, J. S. (1976). Some aspects of the forced wave response of stratified coastal regions. *Journal of Physical Oceanography*, *6*(1), 113–119. https://doi.org/10.1175/1520-0485(1976)006<0113:saotfw>2.0.co;2

Argo. (2021). Argo float data and metadata from Global Data Assembly Centre (Argo GDAC)—Snapshot of Argo GDAC of November 2014 [Dataset]. SEANOE. https://doi.org/10.17882/42182#42281

Bakalian, F. M., Hameed, S., & Pickart, R. (2007). Influence of the Icelandic Low latitude on the frequency of Greenland tip jet events: Implications for Irminger Sea convection. *Journal of Geophysical Research: Oceans*, *112*(4), 1–6. https://doi.org/10.1029/2006jc003807

Böning, C. W., Behrens, E., Biastoch, A., Getzlaff, K., & Bamber, J. L. (2016). Emerging impact of Greenland meltwater on deepwater formation in the North Atlantic Ocean. *Nature Geoscience*, *9*(7), 523–527. https://doi.org/10.1038/ngeo2740

Bower, A. S., Lozier, M. S., Gary, S. F., & Böning, C. W. (2009). Interior pathways of the North Atlantic meridional overturning circulation. *Nature*, *459*(7244), 243–248. https://doi.org/10.1038/nature07979

Brink, K. H. (1982). A comparison of long coastal-trapped wave theory with observations off Peru. *Journal of Physical Oceanography*, *12*(8), 897–913. https://doi.org/10.1175/1520-0485(1982)012<0897:acolct>2.0.co;2

Castelao, R. M., Luo, H., Oliver, H., Rennermalm, A. K., Tedesco, M., Bracco, A., et al. (2019). Controls on the transport of meltwater from the southern Greenland ice sheet in the Labrador Sea. *Journal of Geophysical Research: Oceans*, *124*(6), 3551–3560. https://doi.org/10.1029/2019jc015159

Chanut, J., Barńier, B., Large, W., Debreu, L., Penduff, T., Molines, J. M., & Mathiot, P. (2008). Mesoscale eddies in the Labrador Sea and their contribution to convection and restratification. *Journal of Physical Oceanography*, *38*(8), 1617–1643. https://doi.org/10.1175/2008jpo3485.1

Clarke, A. J. (1977). Observational and numerical evidence for wind-forced coastal trapped long waves. *Journal of Physical Oceanography*, *7*(2), 231–247. https://doi.org/10.1175/1520-0485(1977)007<0231:oanefw>2.0.co;2

Clarke, R. A., & Gascard, J.-C. (1983). The Formation of Labrador Sea Water. Part I: Large-scale processes. *Journal of Physical Oceanography*, *13*(10), 1764–1778. https://doi.org/10.1175/1520-0485(1983)013<1764:tfolsw>2.0.co;2

Colbourne, E. B., Narayanan, S., & Prinsenberg, S. (1994). Climatic changes and environmental conditions in the Northwest Atlantic, 1970–1993. *ICES Marine Science Symposia*, *198*, 311–322.

Cuny, J., Rhines, P. B., Niiler, P. P., & Bacon, S. (2002). Labrador Sea boundary currents and the fate of the Irminger Sea Water. *Journal of Physical Oceanography*, *32*(2), 627–647. https://doi.org/10.1175/1520-0485(2002)032<0627:lsbcat>2.0.co;2

De Jong, M. F., van Aken, H. M., Våge, K., & Pickart, R. S. (2012). Convective mixing in the central Irminger Sea: 2002–2010. *Deep-Sea Research Part I Oceanographic Research Papers*, *63*, 36–51. https://doi.org/10.1016/j.dsr.2012.01.003

Dickson, R., & Brown, J. (1994). The production of North Atlantic Deep Water: Sources, rates, and pathways. *Journal of Geophysical Research*, *99*(C6), 12319–12341. https://doi.org/10.1029/94jc00530

Doyle, J. D., & Shapiro, M. A. (1999). Flow response to large-scale topography: The Greenland tip jet. *Tellus, Series A: Dynamic Meteorology and Oceanography*, *51*(5), 728–748. https://doi.org/10.3402/tellusa.v51i5.14471

Duyck, E., & De Jong, M. F. (2021). Circulation over the south-east Greenland shelf and potential for liquid freshwater export: A drifter study. *Geophysical Research Letters*, *48*(5), 1–9. https://doi.org/10.1029/2020gl091948

Duyck, E., Gelderloos, R., & de Jong, M. F. (2022). Wind-driven freshwater export at Cape Farewell. *Journal of Geophysical Research: Oceans*, *127*(5), e2021JC018309. https://doi.org/10.1029/2021jc018309

Eden, C., & Böning, C. (2002). Sources of eddy kinetic energy in the Labrador Sea. *Journal of Physical Oceanography*, *32*(12), 3346–3363. https://doi.org/10.1175/1520-0485(2002)032<3346:soekei>2.0.co;2

Fischer, J., Visbeck, M., Zantopp, R., & Nunes, N. (2010). Interannual to decadal variability of outflow from the Labrador Sea. *Geophysical Research Letters*, *37*(24), 1–5. https://doi.org/10.1029/2010gl045321

Florindo-López, C., Bacon, S., Aksenov, Y., Chafik, L., Colbourne, E., & Penny Holliday, N. (2020). Arctic Ocean and Hudson Bay freshwater exports: New estimates from seven decades of hydrographic surveys on the Labrador Shelf. *Journal of Climate*, *33*(20), 8849–8868. https://doi.org/10.1175/jcli-d-19-0083.1

Foukal, N. P., Pickart, R. S., Moore, G. W., & Lin, P. (2019). Shelfbreak downwelling in the Alaskan Beaufort Sea. *Journal of Geophysical Research: Oceans*, *124*(10), 7201–7225. https://doi.org/10.1029/2019jc015520

Gascard, J.-C., & Clarke, R. A. (1983). The formation of Labrador Sea Water. Part II: Mesoscale and smaller-scale processes. *Journal of Physical Oceanography*, *13*(10), 1779–1797. https://doi.org/10.1175/1520-0485(1983)013<1779:tfolsw>2.0.co;2

Gelderloos, R., Haine, T. W. N., & Almansi, M. (2021). Coastal trapped waves and other subinertial variability along the southeast Greenland coast in a realistic numerical simulation. *Journal of Physical Oceanography*, *51*(3), 861–877. https://doi.org/10.1175/jpo-d-20-0239.1

Gelderloos, R., Katsman, C. A., & Drijfhout, S. S. (2011). Assessing the roles of three eddy types in restratifying the Labrador Sea after deep convection. *Journal of Physical Oceanography*, *41*(11), 2102–2119. https://doi.org/10.1175/jpo-d-11-054.1

Georgiou, S., Ypma, S. L., Brüggemann, N., Sayol, J.-M., van der Boog, C. G., Spence, P., et al. (2021). Direct and indirect pathways of convected water masses and their impacts on the overturning dynamics of the Labrador Sea. *Journal of Geophysical Research: Oceans*, *126*(1), e2020JC016654. https://doi.org/10.1029/2020jc016654

Group, T. L. S. (1998). The Labrador Sea deep convection experiment. *Bulletin of the American Meteorological Society*, *79*(10), 2033–2058. https://doi.org/10.1175/1520-0477(1998)079<2033:tlsdce>2.0.co;2

Harden, B. E., Renfrew, I. A., & Pickart, R. S. (2014). Offshore transport of dense water from the east Greenland shelf. *Journal of Physical Oceanography*, *44*(1), 229–245. https://doi.org/10.1175/jpo-d-12-0218.1

Harden, B., Straneo, F., & Sutherland, D. (2014). Moored observations of synoptic and seasonal variability in the East Greenland Coastal Current. *Journal of Geophysical Research: OceansOceans*, *119*(12), 8838–8857. https://doi.org/10.1002/2014jc010134

Hátún, H., Eriksen, C. C., & Rhines, P. B. (2007). Buoyant eddies entering the Labrador Sea observed with gliders and altimetry. *Journal of Physical Oceanography*, *37*(12), 2838–2854. https://doi.org/10.1175/2007jpo3567.1

Hersbach, H., Bell, B., Berrisford, P., Biavati, G., Horányi, A., Muñoz Sabater, J., et al. (2018). ERA5 hourly data on single levels from 1959 to present [Dataset]. Copernicus Climate Change Service (C3S) Climate Data Store (CDS). https://doi.org/10.24381/cds.adbb2d47

Hersbach, H., Bell, B., Berrisford, P., Hirahara, S., Horányi, A., Muñoz-Sabater, J., et al. (2020). The ERA5 global reanalysis. *Quarterly Journal of the Royal Meteorological Society*, *146*(730), 1999–2049. https://doi.org/10.1002/qj.3803

Holliday, N. P., Meyer, A., Bacon, S., Alderson, S. G., & de Cuevas, B. (2007). Retroflection of part of the East Greenland Current at Cape Farewell. *Geophysical Research Letters*, *34*(7), L07609. https://doi.org/10.1029/2006gl029085

Huyer, A., Sobey, E. J. C., & Smith, R. L. (1979). The spring transition in currents over the Oregon Continental Shelf. *Journal of Geophysical Research*, *84*(C11), 6995–7011. https://doi.org/10.1029/jc084ic11p06995

Josey, S. A., de Jong, M. F., Oltmanns, M., Moore, G. K., & Weller, R. A. (2019). Extreme variability in Irminger Sea winter heat loss revealed by ocean observatories initiative mooring and the ERA5 reanalysis. *Geophysical Research Letters*, *46*(1), 293–302. https://doi.org/10.1029/2018gl080956

Katsman, C. A., Spall, M. A., & Pickart, R. S. (2004). Boundary current eddies and their role in the restratification of the Labrador Sea. *Journal of Physical Oceanography*, *34*(9), 1967–1983. https://doi.org/10.1175/1520-0485(2004)034<1967:bceatr>2.0.co;2

Kawasaki, T., & Hasumi, H. (2014). Effect of freshwater from the West Greenland Current on the winter deep convection in the Labrador Sea. *Ocean Modeling*, *75*, 51–64. https://doi.org/10.1016/j.ocemod.2014.01.003

Khatiwala, S., Tanhua, T., Mikaloff Fletcher, S., Gerber, M., Doney, S. C., Graven, H. D., et al. (2013). Global ocean storage of anthropogenic carbon. *Biogeosciences*, *10*(4), 2169–2191. https://doi.org/10.5194/bg-10-2169-2013

Lavender, K. L., Davis, R. E., & Owens, W. B. (2000). Middepth recirculation observed in the interior Labrador and Irminger Seas by direct velocity measurements. *Nature*, *407*(6800), 66–69. https://doi.org/10.1038/35024048

Lavender, K. L., Davis, R. E., & Owens, W. B. (2002). Observations of open-ocean deep convection in the Labrador Sea from subsurface floats. *Journal of Physical Oceanography*, *32*(2), 511–526. https://doi.org/10.1175/1520-0485(2002)032<0511:oooodc>2.0.co;2

Lazier, J., Hendry, R., Clarke, A., Yashayaev, I., & Rhines, P. (2002). Convection and restratification in the Labrador Sea, 1990–2000. *Deep-Sea Research Part I Oceanographic Research Papers*, *49*(10), 1819–1835. https://doi.org/10.1016/s0967-0637(02)00064-x

Le Bras, I. A. A., Straneo, F., Holte, J., de Jong, M. F., & Holliday, N. P. (2020). Rapid export of waters formed by convection near the Irminger Sea's Western boundary. *Geophysical Research Letters*, *47*(3), 1–10. https://doi.org/10.1029/2019gl085989

Le Bras, I. A. A., Straneo, F., Holte, J., & Holliday, N. P. (2018). Seasonality of freshwater in the East Greenland Current system from 2014 to 2016. *Journal of Geophysical Research: Oceans*, *123*(12), 8828–8848. https://doi.org/10.1029/2018jc014511

Lentz, S. J., & Chapman, D. C. (2004). The importance of nonlinear cross-shelf momentum flux during wind-driven coastal upwelling. *Journal of Physical Oceanography*, *34*(11), 2444–2457. https://doi.org/10.1175/jpo2644.1

Lilly, J. M., & Rhines, P. B. (2002). Coherent eddies in the Labrador Sea observed from a mooring. *Journal of Physical Oceanography*, *32*(2), 585–598. https://doi.org/10.1175/1520-0485(2002)032<0585:ceitls>2.0.co;2

Lilly, J. M., Rhines, P. B., Schott, F., Lavender, K., Lazier, J., Send, U., & Asaro, E. D. (2003). Observations of the Labrador Sea eddy field. *Progress in Oceanography*, *59*(1), 75–176. https://doi.org/10.1016/j.pocean.2003.08.013

Lilly, J. M., Rhines, P. B., Visbeck, M., Davis, R., Lazier, J. R., Schott, F., & Farmer, D. (1999). Observing deep convection in the Labrador Sea during winter 1994/1995. *Journal of Physical Oceanography*, *29*(8), 2065–2098. https://doi.org/10.1175/1520-0485(1999)029<2065:odcitl>2.0.co;2

Lin, P., Pickart, R. S., Moore, G. W., Spall, M. A., & Hu, J. (2019). Characteristics and dynamics of wind-driven upwelling in the Alaskan Beaufort Sea based on 6 yr of mooring data. *Deep-Sea Research Part II Topical Studies in Oceanography*, *162*, 79–92. https://doi.org/10.1016/j.dsr2.2018.01.002

Lin, P., Pickart, R. S., Stafford, K. M., Moore, G., Torres, D. J., Bahr, F., & Hu, J. (2016). Seasonal variation of the Beaufort shelfbreak jet and its relationship to Arctic cetacean occurrence. *Journal of Geophysical Research: Oceans*, *121*(12), 8434–8454. https://doi.org/10.1002/2016jc011890

Lin, P., Pickart, R. S., Torres, D. J., & Pacini, A. (2018). Evolution of the freshwater coastal current at the Southern Tip of Greenland. *Journal of Physical Oceanography*, *48*(9), 2127–2140. https://doi.org/10.1175/jpo-d-18-0035.1

Lozier, M. S., Li, F., Bacon, S., Bahr, F., Bower, A. S., Cunningham, S. A., et al. (2019). A sea change in our view of overturning in the subpolar North Atlantic. *Science*, *363*(6426), 516–521. https://doi.org/10.1126/science.aau6592

Luo, H., Castelao, R. M., Rennermalm, A. K., Tedesco, M., Bracco, A., Yager, P. L., & Mote, T. L. (2016). Oceanic transport of surface meltwater from the southern Greenland ice sheet. *Nature Geoscience*, *9*(7), 528–532. https://doi.org/10.1038/ngeo2708

Majumder, S., Castelao, R. M., & Amos, C. M. (2021). Freshwater variability and transport in the Labrador Sea from in situ and satellite observations. *Journal of Geophysical Research: Oceans*, *126*(4), 1–17. https://doi.org/10.1029/2020jc016751

Marshall, J., & Schott, F. (1999). Open-ocean convection: Observations, theory, and models. *Reviews of Geophysics*, *37*(98), 1–64. https://doi.org/10.1029/98rg02739

Moore, G. W. (2003). Gale force winds over the Irminger Sea to the east of Cape Farewell, Greenland. *Geophysical Research Letters*, *30*(17), 1–4. https://doi.org/10.1029/2003gl018012

Moore, G. W., Pickart, R. S., & Renfrew, I. A. (2008). Buoy observations from the windiest location in the world ocean, Cape Farewell, Greenland. *Geophysical Research Letters*, *35*(18), 3–7. https://doi.org/10.1029/2008gl034845

Moore, G. W., & Renfrew, I. A. (2005). Tip jets and barrier winds: A QuikSCAT climatology of high wind speed events around Greenland. *Journal of Climate*, *18*(18), 3713–3725. https://doi.org/10.1175/jcli3455.1

Myers, P. G., Donnelly, C., & Ribergaard, M. H. (2009). Structure and variability of the West Greenland Current in summer derived from six repeat standard sections. *Progress in Oceanography*, *80*(1–2), 93–112. https://doi.org/10.1016/j.pocean.2008.12.003

Myers, P. G., Kulan, N., & Ribergaard, M. H. (2007). Irminger water variability in the West Greenland Current. *Geophysical Research Letters*, *34*(17), 2–7. https://doi.org/10.1029/2007gl030419

Ovall, B., Pickart, R. S., Lin, P., Stabeno, P., Weingartner, T., Itoh, M., et al. (2021). Ice, wind, and water: Synoptic-scale controls of circulation in the Chukchi Sea. *Progress in Oceanography*, *199*, 102707. https://doi.org/10.1016/j.pocean.2021.102707

Pacini, A., & Pickart, R. S. (2022). Meanders of the West Greenland Current near Cape Farewell. *Deep-Sea Research Part I Oceanographic Research Papers*, *179*, 103664. https://doi.org/10.1016/j.dsr.2021.103664

Pacini, A., Pickart, R. S., Bahr, F., Torres, D. J., Ramsey, A. L., Holte, J., et al. (2020). Mean conditions and seasonality of the west Greenland boundary current system near Cape Farewell. *Journal of Physical Oceanography*, *50*(10), 2849–2871. https://doi.org/10.1175/jpo-d-20-0086.1

Pacini, A., Pickart, R. S., Le Bras, I. A., Straneo, F., Holliday, N., & Spall, M. (2021). Cyclonic eddies in the west Greenland boundary current system. *Journal of Physical Oceanography*, *51*, 2087–2102. https://doi.org/10.1175/jpo-d-20-0255.1

Pawlowicz, R., Beardsley, B., & Lentz, S. (2002). Classical tidal harmonic analysis including error estimates in MATLAB using TDE. *Computers & Geosciences*, *28*(8), 929–937. https://doi.org/10.1016/s0098-3004(02)00013-4

Pennelly, C., & Myers, P. G. (2020). Introducing LAB60: A 1/60° NEMO 3.6 numerical simulation of the Labrador Sea. *Geoscientific Model Development*, *13*(10), 4959–4975. https://doi.org/10.5194/gmd-13-4959-2020

Pennelly, C., & Myers, P. G. (2021). Impact of different atmospheric forcing sets on modeling Labrador Sea Water production. *Journal of Geophysical Research: Oceans*, *126*(2). https://doi.org/10.1029/2020jc016452

Pickart, R. S. (1992). Water mass components of the North Atlantic deep western boundary current. *Deep-Sea Research Part I: Oceanographic Research Papers*, *39*(9), 1553–1572. https://doi.org/10.1016/0198-0149(92)90047-w

Pickart, R. S. (2018). Microcat, Aquadopp, ADCP, and Tidbit data from the 2014–2016 Labrador Sea eastern boundary mooring array as part of OSNAP (Overturning in the Subpolar North Atlantic Program). [Dataset]. Duke Digital Repository. https://doi.org/10.7924/r4fj2dr7k

Pickart, R. S. (2020). Microcat, Aquadopp, and ADCP data from the 2016–2018 Labrador Sea eastern boundary mooring array as part of OSNAP (Overturning in the Subpolar North Atlantic Program). [Dataset]. Georgia Tech Library. https://doi.org/10.35090/fz80-6c32
Pickart, R. S. (2021). CTD data from Cruise 316N147 [Dataset]. Retrieved from CCHDO https://cchdo.ucsd.edu/cruise/316N147_5
Pickart, R. S. (2022). Conductivity-Temperature-Depth (CTD) data as part of the OSNAP (Overturning in the Subpolar North Atlantic Program), from 2018 on the R/V Neil Armstrong. [Dataset]. Georgia Tech Library. https://doi.org/10.35090/gatech/66765
Pickart, R. S., & Spall, M. A. (2007). Impact of Labrador Sea convection on the North Atlantic meridional overturning circulation. *Journal of Physical Oceanography*, *37*(9), 2207–2227. https://doi.org/10.1175/jpo3178.1
Pickart, R. S., Spall, M. A., & Mathis, J. T. (2013). Dynamics of upwelling in the Alaskan Beaufort Sea and associated shelf-basin fluxes. *Deep-Sea Research Part I Oceanographic Research Papers*, *76*, 35–51. https://doi.org/10.1016/j.dsr.2013.01.007
Pickart, R. S., Spall, M. A., Moore, G. W. K., Weingartner, T. J., Woodgate, R. A., Aagaard, K., & Shimada, K. (2011). Upwelling in the Alaskan Beaufort Sea: Atmospheric forcing and local versus non-local response. *Progress in Oceanography*, *88*(1–4), 78–100. https://doi.org/10.1016/j.pocean.2010.11.005
Pickart, R. S., Spall, M. A., Ribergaard, M. H., Moore, G. W., & Milliff, R. F. (2003). Deep convection in the Irminger Sea forced by the Greenland tip jet. *Nature*, *424*(6945), 152–156. https://doi.org/10.1038/nature01729
Pickart, R. S., Straneo, F., & Moore, G. W. (2003). Is Labrador Sea Water formed in the Irminger basin? *Deep-Sea Research Part I Oceanographic Research Papers*, *50*(1), 23–52. https://doi.org/10.1016/s0967-0637(02)00134-6
Pickart, R. S., Torres, D. J., & Clarke, R. A. (2002). Hydrography of the Labrador Sea during active convection. *Journal of Physical Oceanography*, *32*(2), 428–457. https://doi.org/10.1175/1520-0485(2002)032<0428:hotlsd>2.0.co;2
Piron, A., Thierry, V., Mercier, H., & Caniaux, G. (2017). Gyre-scale deep convection in the subpolar North Atlantic Ocean during winter 2014–2015. *Geophysical Research Letters*, *44*(3), 1439–1447. https://doi.org/10.1002/2016gl071895
Prater, M. D. (2002). Eddies in the Labrador Sea as observed by profiling RAFOS floats and remote sensing. *Journal of Physical Oceanography*, *32*(2), 411–427. https://doi.org/10.1175/1520-0485(2002)032<0411:eitlsa>2.0.co;2
Price, J. F., Weller, R. A., & Pinkel, R. (1986). Diurnal cycling: Observations and models of the upper ocean response to diurnal heating, cooling, and wind mixing. *Journal of Geophysical Research*, *91*(C7), 8411–8427. https://doi.org/10.1029/jc091ic07p08411
Renfrew, I. A., Moore, G. W., Guest, P. S., & Bumke, K. (2002). A comparison of surface layer and surface turbulent flux observations over the Labrador Sea with ECMWF analyses and NCEP reanalyses. *Journal of Physical Oceanography*, *32*(2), 383–400. https://doi.org/10.1175/1520-0485(2002)032<0383:acosla>2.0.co;2
Renfrew, I. A., Peterson, G., Sproson, D., Moore, G., Adiwidjaja, H., Zhang, S., & North, R. (2009). A comparison of aircraft-based surface-layer observations over Denmark Strait and the Irminger Sea with meteorological analyses and QuikSCAT winds. *Quarterly Journal of the Royal Meteorological Society*, *135*(645), 2046–2066. https://doi.org/10.1002/qj.444
Rhein, M., Fischer, J., Smethie, W. M., Smythe-Wright, D., Weiss, R. F., Mertens, C., et al. (2002). Labrador Sea water: Pathways, CFC inventory, and formation rates. *Journal of Physical Oceanography*, *32*(2), 648–665. https://doi.org/10.1175/1520-0485(2002)032<0648:lswpci>2.0.co;2
Rieck, J. K., Böning, C. W., & Getzlaff, K. (2019). The nature of eddy kinetic energy in the Labrador Sea: Different types of mesoscale eddies, their temporal variability, and impact on deep convection. *Journal of Physical Oceanography*, *49*(8), 2075–2094. https://doi.org/10.1175/jpo-d-18-0243.1
Rogers, J. C. (1990). Patterns of low-frequency monthly sea level pressure variability (1899–1986) and associated wave cyclone frequencies. *Journal of Climate*, *3*(12), 1364–1379. https://doi.org/10.1175/1520-0442(1990)003<1364:polfms>2.0.co;2
Rykova, T., Straneo, F., & Bower, A. S. (2015). Seasonal and interannual variability of the West Greenland Current System in the Labrador Sea in 1993–2008. *Journal of Geophysical Research: Oceans*, *120*(2), 1318–1332. https://doi.org/10.1002/2014jc010386
Sampe, T., & Xie, S. P. (2007). Mapping high sea winds from space: A global climatology. *Bulletin of the American Meteorological Society*, *88*(12), 1965–1978. https://doi.org/10.1175/bams-88-12-1965
Schulze, L. M., & Pickart, R. S. (2012). Seasonal variation of upwelling in the Alaskan Beaufort Sea: Impact of sea ice cover. *Journal of Geophysical Research: Oceans*, *117*(6), 1–19. https://doi.org/10.1029/2012jc007985
Schulze, L. M., Pickart, R. S., & Moore, G. (2016). Atmospheric forcing during active convection in the Labrador Sea and its impact on mixed-layer depth. *Journal of Geophysical Research: Oceans*, *121*(9), 6978–6992. https://doi.org/10.1002/2015jc011607
Schulze Chretien, L. M., & Frajka-Williams, E. (2018). Wind-driven transport of fresh shelf water into the upper 30 m of the Labrador Sea. *Ocean Science*, *14*(5), 1247–1264. https://doi.org/10.5194/os-14-1247-2018
Serreze, M. C., Carse, F., Barry, R. G., & Rogers, J. C. (1997). Icelandic low cyclone activity: Climatological features, linkages with the NAO, and relationships with recent changes in the Northern Hemisphere circulation. *Journal of Climate*, *10*(3), 453–464. https://doi.org/10.1175/1520-0442(1997)010<0453:ilcacf>2.0.co;2
Smith, W. H. F., & Wessel, P. (1990). Gridding with continuous curvature splines in tension. *Geophysics*, *55*(3), 293–305. https://doi.org/10.1190/1.1442837
Sofianos, S. S., & Johns, W. E. (2001). Wind induced sea level variability in the Red Sea. *Geophysical Research Letters*, *28*(16), 3175–3178. https://doi.org/10.1029/2000gl012442
Straneo, F. (2006). Heat and freshwater transport through the central Labrador Sea. *Journal of Physical Oceanography*, *36*(4), 606–628. https://doi.org/10.1175/jpo2875.1
Sy, A., Rheint, M., Lazier, J. R., Koltermann, K. P., Meincke, J., Putzka, A., & Bersch, M. (1997). Surprisingly rapid spreading of newly formed intermediate waters across the North Atlantic Ocean. *Nature*, *386*(6626), 675–679. https://doi.org/10.1038/386675a0
Takahashi, T., Sutherland, S. C., Wanninkhof, R., Sweeney, C., Feely, R. A., Chip-man, D. W., et al. (2009). Climatological mean and decadal change in surface ocean pCO_2, and net sea-air CO_2 flux over the global oceans. *Deep-Sea Research Part II Topical Studies in Oceanography*, *56*(8–10), 554–577. https://doi.org/10.1016/j.dsr2.2008.12.009
Talley, L., & McCartney, M. (1982). Distribution and circulation of Labrador Sea Water. *Journal of Physical Oceanography*, *12*(11), 1189–1205. https://doi.org/10.1175/1520-0485(1982)012<1189:dacols>2.0.co;2
Thomsen, S., Carsten, E., & Czeschel, L. (2014). Stability analysis of the Labrador Current. *Journal of Physical Oceanography*, *44*(2), 445–463. https://doi.org/10.1175/jpo-d-13-0121.1
Våge, K., Pickart, R. S., Moore, G. W., & Ribergaard, M. H. (2008). Winter mixed layer development in the central Irminger Sea: The effect of strong, intermittent wind events. *Journal of Physical Oceanography*, *38*(3), 541–565. https://doi.org/10.1175/2007jpo3678.1

Våge, K., Spengler, T., Davies, H. C., & Pickart, R. S. (2009). Multi-event analysis of the westerly Greenland tip jet based upon 45 winters in ERA-40. *Quarterly Journal of the Royal Meteorological Society*, *135*(645), 1999–2011. https://doi.org/10.1002/qj.488

Yashayaev, I., & Loder, J. W. (2016). Recurrent replenishment of Labrador Sea Water and associated decadal-scale variability. *Journal of Geophysical Research: Oceans*, *121*(8), 8095–8114. https://doi.org/10.1002/2016jc012046

Zunino, P., Mercier, H., & Thierry, V. (2020). Why did deep convection persist over four consecutive winters (2015–2018) southeast of Cape Farewell? *Ocean Science*, *16*(1), 99–113. https://doi.org/10.5194/os-16-99-2020